

# Star(bursts) of FIRE: observational signatures of bursty star formation in galaxies

Martin Sparre<sup>1,2,\*†</sup>, Christopher C. Hayward<sup>3,4‡</sup>, Robert Feldmann<sup>5§</sup>, Claude-André Faucher-Giguère<sup>6</sup>, Alexander L. Muratov<sup>7</sup>, Dušan Kereš<sup>7</sup>, Philip F. Hopkins<sup>3</sup>

<sup>1</sup>Heidelberger Institut für Theoretische Studien, Schloss-Wolfsbrunnenweg 35, 69118 Heidelberg, Germany

<sup>2</sup>Dark Cosmology Centre, Niels Bohr Institute, University of Copenhagen, Juliane Maries Vej 30, 2100 Copenhagen, Denmark

<sup>3</sup>TAPIR 350-17, California Institute of Technology, 1200 E. California Boulevard, Pasadena, CA 91125, USA

<sup>4</sup>Harvard-Smithsonian Center for Astrophysics, 60 Garden Street, Cambridge, MA 02138, USA

<sup>5</sup>Department of Astronomy, University of California, Berkeley, CA 94720-3411, USA

<sup>6</sup>Department of Physics and Astronomy and CIERA, Northwestern University, 2145 Sheridan Road, Evanston, IL 60208, USA

<sup>7</sup>Department of Physics, Center for Astrophysics and Space Science, University of California at San Diego, 9500 Gilman Drive, La Jolla, CA 92093, USA

29 January 2022

## ABSTRACT

Galaxy formation models exhibit remarkable success in reproducing observed relations such as the relation between galaxies’ star formation rates (SFRs) and stellar masses ( $M_*$ ) and the stellar mass–halo mass relation. We demonstrate that comparisons of the short-timescale variability in galaxy SFRs with observational data provide an additional useful constraint on the physics of galaxy formation feedback. We apply SFR indicators with different sensitivity timescales to galaxies from the Feedback in Realistic Environments (FIRE) simulations. We find that the SFR– $M_*$  relation has a significantly greater scatter when the H $\alpha$ -derived SFR is considered compared with when the far-ultraviolet (FUV)-based SFR is used. This difference is a direct consequence of bursty star formation because the FIRE galaxies exhibit order-of-magnitude SFR variations over timescales of a few Myr. Consequently, low-mass galaxies can go through both quenched (in terms of the 10-Myr averaged SFR) and starburst phases within a 200-Myr period. We also find that the H $\alpha$ /FUV ratios are very similar to those observed for local galaxies, although there is a population of simulated galaxies with lower H $\alpha$ /FUV ratios than observed at  $M_* \lesssim 10^{9.5} M_\odot$ . The interpretation is that our sample of FIRE galaxies is slightly more bursty than the observed sample of galaxies in the vicinity of the Galaxy. A possible explanation is that despite the very high resolution of the simulations, the SFR variability and thus H $\alpha$ /FUV ratios may not be fully converged. We suggest that future cosmological simulations should compare the H $\alpha$ /FUV ratios of their galaxies with observations to constrain the feedback models employed.

**Key words:** cosmology: theory – methods: numerical – galaxies: evolution – galaxies: formation – galaxies: star formation – galaxies: starburst.

## 1 INTRODUCTION

Most massive spiral galaxies in the present-day Universe are in a quasi-equilibrium in which the formation and destruction of giant molecular clouds (GMCs), and the subsequent formation of stars, are regulated by various feedback processes and the infall of gas (Kereš et al. 2005). For example, the Galaxy is in a steady state in which stars are formed at a constant rate of  $\simeq 1 M_\odot \text{yr}^{-1}$  (Robitaille & Whitney 2010; Chomiuk & Povich 2011). However,

some galaxies appear to be out of equilibrium in the sense that they are forming stars so rapidly that they will deplete their gas reservoirs on timescales of 10 – 100 Myr (Rodighiero et al. 2011; Atek et al. 2011, 2014; Maseda et al. 2014). Such galaxies are referred to as *starburst* galaxies.<sup>1</sup> The definition of a starburst often involves the concept of a timescale – typically either the gas

<sup>1</sup> It is worth noting that the term ‘starburst’ is an ambiguous concept that is used in many ways in the literature; see Knapen & James (2009) for a thorough discussion. For this reason, one should use caution when comparing our results to the literature, especially that of the high-redshift galaxy community, in which the term ‘starburst’ is often used to mean ‘a galaxy with a high SFR’.

\* E-mail: sparre@dark-cosmology.dk

† Sapere Aude Fellow

‡ Moore Prize Postdoctoral Scholar in Theoretical Astrophysics

§ Hubble Fellow

consumption timescale ( $M_{\text{gas}}/\text{SFR}$ ) or the stellar mass doubling timescale ( $M_*/\text{SFR}$ ) – that is short compared to the lifetime of the galaxy (Knapen & James 2009). An alternative definition of a starburst relies on comparing SFR indicators that are sensitive to different timescales. For example, the  $\text{H}\alpha$  nebular emission line and UV continuum fluxes typically trace a galaxy’s SFR averaged over the last  $\simeq 10$  and  $\simeq 200$  Myr, respectively (Kennicutt & Evans 2012; Calzetti 2013). Thus, if a galaxy has an increased  $\text{H}\alpha/\text{UV}$  flux ratio compared to the overall population of galaxies, this galaxy may have had a short burst of star formation within the last 10 Myr. Observations of  $\text{H}\alpha$ - and UV-derived SFRs indeed show that short ( $\simeq 10$  Myr) bursts play an important role in local dwarf galaxies (Weisz et al. 2012). A similar conclusion was reached in a study of galaxies from the Sloan Digital Sky Survey (Kauffmann 2014). Both studies found a starburst fraction that decreases with increasing stellar mass.

Establishing the role of bursty star formation is important for various reasons. For example, a potential physically important consequence of bursty star formation is that it may be able to transform dark matter cusps into cores (Pontzen & Governato 2012; Di Cintio et al. 2014; Oñorbe et al. 2015; Chan et al. 2015; Read et al. 2015). However, there is an ongoing debate whether the amount of energy that must be deposited into the interstellar medium (ISM) for this transition to occur is realistic (Garrison-Kimmel et al. 2013; Amorisco et al. 2014), and recent simulations also suggest that how effective bursty star formation is at transforming cusps into cores strongly depends on when in a halo’s evolutionary history the energy injection occurs (Oñorbe et al. 2015; Chan et al. 2015). Starbursts can also have important consequences for generation of galactic outflows (e.g. Heckman et al. 1990; Martin 1998, 2005; Thompson et al. 2005; Hopkins et al. 2013b; Muratov et al. 2015), metal enrichment of the ISM (Tremonti et al. 2004; Erb et al. 2006; Torrey et al. 2012), and formation of globular clusters (Sanders & Mirabel 1996; Portegies Zwart et al. 2010), among other topics.

Understanding the time variability of galaxy star formation histories is also critical for many observational reasons. For example, it has been shown that bursty star formation can potentially bias high-redshift galaxy surveys because galaxies in an active burst state will be preferentially selected (Domínguez et al. 2015). Also, spectral energy distribution modeling is routinely used to infer physical properties of galaxies (see Walcher et al. 2011 and Conroy 2013 for recent reviews). Because the results of such modeling can be quite sensitive to the star formation histories used to generate the model library (e.g., Pacifici et al. 2013, 2015; Michałowski et al. 2014; Simha et al. 2014; Smith & Hayward 2015), it is desirable that the input star formation histories are as physically motivated as possible.

Large-volume cosmological simulations of galaxy formation must rely on ‘sub-resolution’ models (Springel & Hernquist 2003; Oppenheimer & Davé 2006; Scannapieco et al. 2012; Dalla Vecchia & Schaye 2012) because the sub-kiloparsec structure of the ISM is not resolved. Instead, stars are stochastically formed at a rate determined by the local gas density, and a self-regulated ISM is achieved by imposing an effective equation of state that attempts to account for unresolved feedback processes. Examples of state-of-the-art simulations that use such sub-resolution physics models include the Illustris (Vogelsberger et al. 2014), EAGLE (Schaye et al. 2015) and MassiveBlack-II (Khandai et al. 2015) simulations. In contrast, several recent simulations have attempted to physically model the effects of feedback on star-forming clouds instead of imposing a sub-resolution description of them (Stinson et al. 2006; Mashchenko et al. 2008; Governato et al. 2010; Zolotov et al. 2012;

Teyssier et al. 2013). The star formation histories of galaxies simulated with explicit ‘resolved’ feedback are typically more bursty than when a sub-resolution ISM model is used; the latter typically result in a SFR variability timescale of  $\gtrsim 100$  Myr (Sparre et al. 2015). However, no galaxy simulations include first-principle calculations of feedback, and there is thus always some uncertainty inherent in the parameterisations or implementations of feedback processes. Consequently, it is a priori unknown whether the very bursty star formation histories of resolved-feedback simulations or the smoother star formation histories of sub-resolution ISM models are more representative of reality. Thus, if feasible, comparisons of the burstiness of simulated and real galaxies’ star formation histories may provide an important diagnostic that can inform feedback models.

The *Feedback in Realistic Environments* (FIRE; Hopkins et al. 2014) project simulates galaxies in cosmological environments with a model for explicit stellar feedback. In the FIRE simulations, energy and momentum input from young stars and SN explosions are directly calculated using a stellar population synthesis model. Feedback operates on the scales of star-forming clouds within the ISM, without artificial ingredients such as suppressed cooling and hydrodynamical decoupling that are often used in other cosmological simulations. The FIRE simulations are also some of the highest-resolution cosmological simulations at a given mass that have been performed to date. The physical model for stellar feedback used in the FIRE simulations has successfully produced star-forming galaxies that obey the Kennicutt–Schmidt relation (Kennicutt 1998; Schmidt 1959), which relates the gas and SFR surface densities of galaxies. The simulations also exhibit good agreement with the stellar mass – halo mass ratio inferred from abundance matching and the observed  $\text{SFR}-M_*$  relation in the local Universe. Given the FIRE model’s success in reproducing these observational constraints, it is natural to consider which tests can further constrain the physical fidelity of the model.

The aim of this paper is to characterise the time variability of star formation in a suite of cosmological ‘zoom-in’ simulations from the FIRE project (Hopkins et al. 2014). By modeling the behaviour of different SFR indicators, it will be tested whether the burstiness of the FIRE galaxies is consistent with observations of real galaxies. The remainder of this paper is organised as follows. Section 2 introduces the different SFR indicators considered, and Section 3 summarises the details of the simulations used in this work. Section 4 studies population-based measures of bursty star formation, including the  $\text{SFR}-M_*$  relation and quenched and starburst fractions. Section 5 characterises the time variability of individual galaxies’ star formation histories, presents an observational comparison, and Section 6 reveals the physical mechanism that drives the burstiness of the simulated galaxies’ star formation histories. Section 7 discusses some implications of our results and observational evidence that suggests that bursty star formation histories are common amongst real galaxies. Section 8 summarises the primary conclusions of this work.

## 2 STAR FORMATION RATE INDICATORS

To introduce the concept of bursty star formation histories, we study the responses of four different SFR indicators to a rapid change in a galaxy’s SFR. We examine a steady star-forming galaxy in which a 20-Myr-long burst that increases the SFR by a factor of

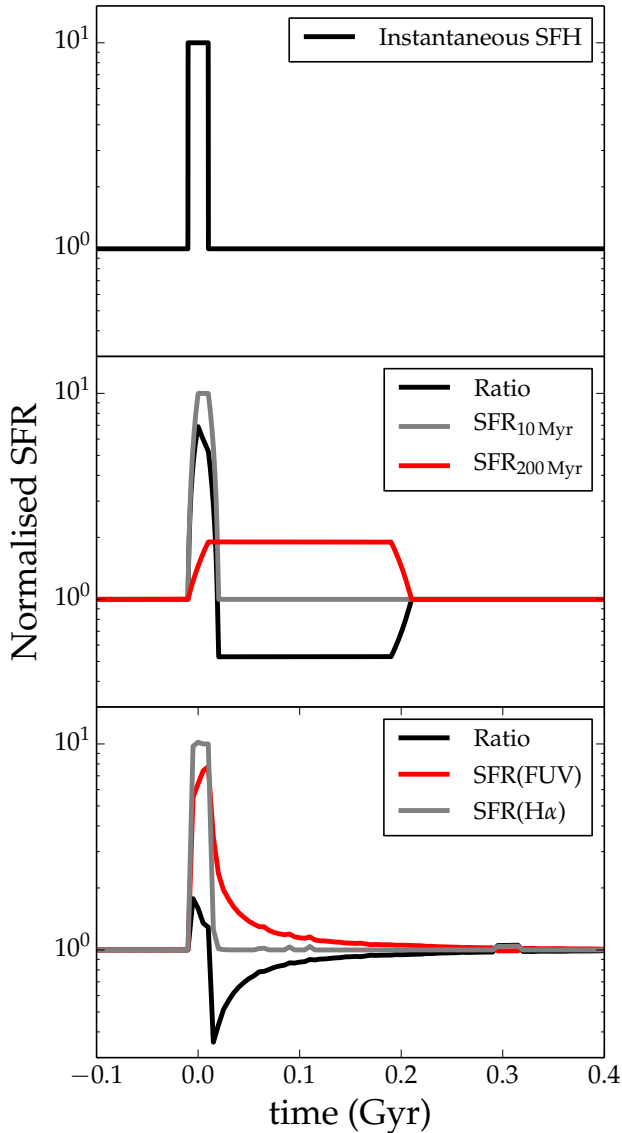


**Figure 1.** The response of four different SFR indicators to the instantaneous star formation history given by Equation (1), which is shown in the *upper panel*. The *middle panel* shows the SFR averaged over the past 10 and 200 Myr and the ratio of these two values, and the *lower panel* shows the behaviour of the SFRs derived from the  $H\alpha$  nebular flux and the FUV continuum and their ratio. The figure shows that the ratios  $SFR_{10\text{ Myr}}/SFR_{200\text{ Myr}}$  and  $SFR(H\alpha)/SFR(FUV)$  are sensitive to the presence of short-timescale SFR variability.

10 occurs:

$$SFR = \begin{cases} 10 M_{\odot}\text{yr}^{-1} & \text{if } |t| < 10 \text{ Myr,} \\ 1 M_{\odot}\text{yr}^{-1} & \text{otherwise.} \end{cases} \quad (1)$$

First, we consider two theoretical indicators,  $SFR_{10\text{ Myr}}$  and  $SFR_{200\text{ Myr}}$ , which correspond to the SFR of a galaxy averaged over the preceding 10 and 200 Myr, respectively. We also consider two observationally motivated SFR indicators:  $SFR(H\alpha)$ , the SFR inferred from the  $H\alpha$  recombination line luminosity, and the SFR inferred from the far-ultraviolet (FUV) continuum luminosity,  $SFR(FUV)$ . We now describe how we calculate  $SFR(H\alpha)$  and  $SFR(FUV)$  via stellar synthesis modelling.

## 2.1 Stellar synthesis modeling with the SLUG code

In our modeling, we use the SLUG code (da Silva et al. 2012, 2014; Krumholz et al. 2015), which, given a star formation history, calculates the spectral energy distribution of a galaxy. To calculate the spectrum, we input the star formation history of a galaxy over the past 200 Myr. The  $H\alpha$  and FUV fluxes from stellar populations older than 200 Myr are negligible, so it is unnecessary to consider the SFH at longer look-back times. We assume the stellar population to follow solar-metallicity Geneva-tracks with no rotation (Ekström et al. 2012). The stellar atmospheres are treated as in STARBURST99 (Leitherer et al. 1999; Vázquez & Leitherer 2005; Leitherer et al. 2010, 2014), in which OB star atmospheres are from Pauldrach et al. (2001), Wolf-Rayet star atmospheres are from Hillier & Miller (1998), and all other stellar atmospheres are from Lejeune et al. (1997). We assume a fully sampled Kroupa (2001) initial mass function (IMF). To derive a UV-based SFR, we calculate the flux of the stellar continuum transmitted through the GALEX FUV filter. We assume that the  $H\alpha$ -derived SFR is proportional to the flux of ionizing photons. With these choices, we can directly compare with  $H\alpha$ - and FUV-derived SFRs and  $H\alpha/FUV$  flux ratios. We make no attempt to model dust attenuation in the present work; thus, our predictions should be compared with dust-corrected observations.

## 2.2 The behaviour of the four different SFR indicators

Figure 1 shows the star formation history specified by Equation (1) together with the time evolution of the four different SFR indicators that we consider.  $SFR_{10\text{ Myr}}$  has a fast response to the change in the instantaneous SFR and is a good indicator of the actual SFR of the galaxy.  $SFR_{200\text{ Myr}}$  has a slower response, and the maximum SFR elevation (relative to the steady-state SFR) according to this indicator is only a factor of 2. The ratio  $SFR_{10\text{ Myr}}/SFR_{200\text{ Myr}}$  is very sensitive to the burstiness of a galaxy’s star formation history. During the 20 Myr of the burst, this quantity is significantly elevated above the equilibrium value for a constant SFR (the equilibrium value is 1.0 with our choice of normalisation), and in the 200 Myr after the burst, it is smaller than this equilibrium value, since  $SFR_{200\text{ Myr}}$  is still affected by the burst until this time. The statistical distribution of  $SFR_{10\text{ Myr}}/SFR_{200\text{ Myr}}$  for a sample of galaxies is therefore an efficient way to measure the importance of short-timescale bursts: galaxies undergoing a short timescale burst have  $SFR_{10\text{ Myr}}/SFR_{200\text{ Myr}} > 1$ , and galaxies that have experienced a burst at lookback times of  $10\text{ Myr} < t < 200\text{ Myr}$  have  $SFR_{10\text{ Myr}}/SFR_{200\text{ Myr}} < 1$ . We refer to the latter galaxies as being in a *post-burst* phase.

The timescales to which the  $H\alpha$ - and FUV-derived SFRs are sensitive are of order 10 and 200 Myr, respectively, although their responses to changes in the SFR are non-linear because of various aspects of the stellar synthesis modeling (e.g. evolution of massive stars over the timescales probed). Qualitatively,  $SFR(H\alpha)/SFR(FUV)$  is similar to  $SFR_{10\text{ Myr}}/SFR_{200\text{ Myr}}$ , since it is larger during the burst and smaller in the post-burst phase. A difference between  $SFR_{10\text{ Myr}}/SFR_{200\text{ Myr}}$  and  $SFR(H\alpha)/SFR(FUV)$  is that the time-averaged values of the ratios are 1.08 and 0.89, respectively, during the time where the ratios are affected by the burst,  $-10\text{ Myr} < t < 210\text{ Myr}$ . The median values of the two ratios are 0.53 and 0.90, respectively. Bursts of star formation will therefore not only increase the scatter in the ratio of two SFR indicators with different timescales but also affect the overall time-averaged and median values of the ratio.

Simulation name	$m_b$ $M_\odot$	$\epsilon_b$ pc	$m_{dm}$ $M_\odot$	$\epsilon_{dm}$ pc	$z$	Sample A #	Sample B #	Note
m10	$2.6 \times 10^2$	3	$1.3 \times 10^3$	30	0.0, 0.2, 0.4	3	3	
m11	$7.1 \times 10^3$	7	$3.5 \times 10^4$	70	0.0, 0.2, 0.4	9	13	
m12i	$5.0 \times 10^4$	14	$2.8 \times 10^5$	140	0.0, 0.2, 0.4	16	24	
m12q	$7.1 \times 10^3$	10	$2.8 \times 10^5$	140	0.0, 0.2, 0.4	5	11	
m12v	$3.9 \times 10^4$	10	$2.0 \times 10^5$	140	2	-	-	used in Sec. 6
MassiveFIRE – HR	$3.3 \times 10^4$	9	$1.7 \times 10^5$	143	2	786	5760	
MassiveFIRE – SR	$2.7 \times 10^5$	9	$1.4 \times 10^6$	143	2	-	-	used in Sec. 5.4
FG15	$5.9 \times 10^4$	9	$2.9 \times 10^5$	143	2	142	187	

**Table 1.** Details of the zoom-in simulations used in this paper. The table includes the baryonic mass resolution ( $m_b$ ), the minimum physical baryonic softening length ( $\epsilon_b$ ), the dark matter mass resolution ( $m_{dm}$ ), the minimum physical dark matter softening length ( $\epsilon_{dm}$ ), the redshift at which the simulation is analysed in this paper, and the number of galaxies in samples A and B (see Section 3.3).

In the remaining parts of this paper, we will use  $SFR_{10\text{ Myr}}$  and  $SFR_{200\text{ Myr}}$  to gain theoretical insight into the SFR variability of the simulated galaxies, and we will use  $SFR(H\alpha)/SFR(FUV)$  when comparing directly to observations.

### 3 OVERVIEW OF THE FIRE SIMULATIONS

The goal of the FIRE project<sup>2</sup> (Hopkins et al. 2014) is to understand how feedback (thus far only stellar feedback) regulates the formation of galaxies in the  $\Lambda$ CDM cosmology. The code used for the simulations analysed in this work is a heavily modified version of the GADGET code (Springel et al. 2001; Springel 2005), GIZMO (Hopkins 2014, 2015).<sup>3</sup> The hydrodynamical equations were solved with the pressure-based formulation of the smoothed particle hydrodynamics method (Hopkins 2013).

The simulations are performed using a multi-scale (‘zoom-in’) technique in which the resolution is high near the galaxy of interest and the structure on larger scales is more coarsely resolved. The dark matter is modeled using collisionless particles. Gas cools according to a cooling function that includes contributions from gas in ionized, atomic, and molecular phases. We follow chemical abundances of nine metal species (C, N, O, Ne, Mg, Si, S, Ca and Fe), with enrichment following each source of mass return individually. During the course of the hydrodynamical calculation, ionization balance of all tracked elements is computed using the ultraviolet background model of Faucher-Giguère et al. (2009), and we apply an on-the-fly approximation for self-shielding of dense gas. The molecular fraction of dense gas is calculated following Krumholz & Gnedin (2011). Stars are formed from molecular gas that has a number density  $n > 10 - 100\text{ cm}^{-3}$  and is locally self-gravitating, and an efficiency of 100% per free-fall time is assumed; see Hopkins et al. (2014) for details.

The star particles that are formed from star-forming gas are treated as single-age stellar populations, for which a fully sampled Kroupa IMF (Kroupa 2001) is assumed. Stellar feedback in the form of radiation pressure, supernovae, stellar winds, photoionization, and photoelectric heating is included. The inputs for the feedback models (such as stellar luminosity and supernova rates) are taken directly from STARBURST99 (Leitherer et al. 1999; Vázquez & Leitherer 2005; Leitherer et al. 2010, 2014). We refer the reader to Hopkins et al. (2011, 2012) for details regarding and extensive tests of the stellar feedback models and to Hopkins et al. (2014) for

details of the stellar feedback model as implemented in the FIRE simulations.

Several earlier works have studied the behaviour of galaxies formed with the FIRE physics model. Muratov et al. (2015) studied the properties of the galactic outflows that are self-consistently generated by stellar feedback in the FIRE simulations. Among other results, they found that the wind mass-loading factors ( $\eta$ , the mass outflow rate divided by the SFR) decrease with stellar mass as  $\eta \propto M_*^{-0.351}$  independently of redshift, except for massive galaxies ( $M_* > 10^{10} M_\odot$ ), for which the mass-loading factors are effectively zero at  $z \lesssim 1$ . Faucher-Giguère et al. (2015) found that the strong galactic winds generated by the simulated FIRE galaxies predict covering fractions of dense neutral hydrogen in good agreement with observational constraints around star-forming galaxies at  $z \simeq 2$ . Other topics studied are the structure and substructure of dwarf-galaxies (Wheeler et al. 2015), the mass – metallicity relation (Ma et al. 2015a) and the Ly $\alpha$  escape fraction at high redshift (Ma et al. 2015b).

#### 3.1 $z = 0$ simulations: The fiducial FIRE simulations

To study the burstiness of galaxies at low redshift, we use the m10, m11, m12i and m12q runs from Hopkins et al. (2014); see Table 1 for details of these simulations. In order to compute e.g. the H $\alpha$ -derived SFR accurately, we need a high number of star particles formed per unit time (this is further described in section 3.3), which means that we can calculate this quantity reliably for only a few halos per simulation snapshot. When studying the burstiness of galaxies at low redshift, we therefore build a sample of galaxies that contains all the well-sampled halos from the above simulations from the time snapshots at  $z = 0$ ,  $z = 0.2$  and  $z = 0.4$ . By choosing these three redshifts, it is ensured that the 200-Myr time intervals from the different snapshots do not overlap, and the galaxies from these snapshots are all from a cosmic epoch well after the peak of the global SFR density at  $z \simeq 2$  (Hopkins & Beacom 2006; Ilbert et al. 2013; Behroozi et al. 2013). In figure legends we will simply refer to the galaxies at  $z = 0$ ,  $z = 0.2$  and  $z = 0.4$  as ‘ $z = 0$  galaxies’.

#### 3.2 $z = 2$ simulations

To build a sample of galaxies at  $z = 2$ , we use the MassiveFIRE simulation suite (Feldmann et al., in prep.) and the set of  $z2hXXX$  simulations from Faucher-Giguère et al. (2015). We will refer to the latter set of simulations as FG15. The simulations in both suites were performed with high mass resolution and thus were only run until  $z = 2$  in order to make it possible to run a

<sup>2</sup> The FIRE website is <http://fire.northwestern.edu/>.

<sup>3</sup> A public version of GIZMO can be downloaded from [www.tapir.caltech.edu/~phopkins/Site/GIZMO.html](http://www.tapir.caltech.edu/~phopkins/Site/GIZMO.html).

large sample of simulations. Our sample of halos from the MassiveFIRE suite comes from 15 high-resolution (HR) and 9 standard resolution (SR) cosmological zoom-in simulations of halos with  $M_{200} \simeq 2 \times 10^{12} - 3 \times 10^{13} M_{\odot}$  using the same feedback model as the simulations presented in Hopkins et al. (2014). The HR runs have a significantly increased resolution compared with the  $10^{13} M_{\odot}$  halo presented in Hopkins et al. (2014), which we do not analyze in this work; see the details presented in Table 1. The  $z2hXXX$  simulations from Faucher-Giguère et al. (2015) were originally performed for the purpose of studying the gas properties of Lyman-break galaxies at  $z = 2$ . These halos have a similar mass resolution as MassiveFIRE but lower halo masses; we will therefore use galaxies from both the MassiveFIRE and FG15 simulation suites when studying the properties of  $z = 2$  galaxies in the upcoming sections.

### 3.3 Identification of galaxies and determination of their star formation histories

Most of the analysis in this paper relies on star formation histories of galaxies. As discussed in Section 2, the burstiness of a star formation history can be quantified by comparing the SFRs averaged over 10 Myr and 200 Myr,  $\text{SFR}_{10 \text{ Myr}}$  and  $\text{SFR}_{200 \text{ Myr}}$ , or the observational analogues,  $\text{SFR}(\text{H}\alpha)$  and  $\text{SFR}(\text{FUV})$ . To calculate the star formation histories of the galaxies in the FIRE simulations listed in Table 1, we first identify halos and subhalos using the AMIGA halo finder (Gill et al. 2004; Knollmann & Knebe 2009). To avoid significant contamination from low-resolution particles, we require galaxies to have a mass fraction of high-resolution particles of  $f_{\text{ hires}} > 0.9$  and containing at least 1000 stellar population particles. The stellar component of the galaxy is defined as all star particles within 20% of the virial radius.

We define a sample of galaxies with well-sampled star formation histories, which later is used to study different star formation rate indicators, and we also define a sample of all galaxies, which will be used to study quenched fractions:

#### Sample A: Galaxies with well-sampled star formation histories

To build a sample of galaxies with well-sampled star formation histories within the last 200 Myr before a given time we include all galaxies with more than 50 stars formed within 20% of the virial radius in the last 200 Myr. Note, that requiring 50 stars to have formed within the last 200 Myr of a snapshot biases the sample towards star-forming galaxies, since it excludes galaxies with  $\text{SFR} < 50 \times m_{*}/(200 \text{ Myr})$ , where  $m_{*}$  is the mean mass of a star particle in a simulation. This sample includes both central galaxies and satellites.

We then calculate the star formation history over the past 200 Myr based on the age distribution of the stellar particles. When calculating the ratio between two SFR indicators we assume all stellar particles to have identical masses at formation time, and when calculating the actual SFR based on an indicator we correct for the stellar mass loss by assuming that stellar populations have lost 10% (25%) of their mass due to stellar evolution in the first 10 Myr (200 Myr) after their formation time (following Fig. 106 in Leitherer et al. 1999).

When our analysis requires calculation of the  $\text{H}\alpha$ -derived SFR, we require the star formation histories to never be lower than  $50 \times m_{*}/(200 \text{ Myr})$ . This requirement is used to avoid galaxies with zero  $\text{H}\alpha$ -flux, which would otherwise arise if no stars are formed within the 10 Myr prior to a snapshot.

**Sample B: All galaxies** We also build a sample of all galaxies with more than 1000 star particles identified by the halo finder, independent of whether they have well-sampled star formation histories or not.

At  $z = 0$  the galaxies in our samples are selected from m10, m11, m12i and m12q, and at  $z = 2$  the galaxies are from the MassiveFIRE – HR runs and FG15 simulations. The number of galaxies in sample A and B from each simulation is quoted in Table 1.

## 4 POPULATION-BASED MEASURES OF BURSTY STAR FORMATION

### 4.1 The SFR – $M_{*}$ relation

Multi-wavelength observations indicate the presence of a correlation between the SFRs and stellar masses,  $M_{*}$ , of star-forming galaxies at fixed redshift, and the normalisation of this relation increases with increasing redshift (Brinchmann et al. 2004; Elbaz et al. 2011; Rodighiero et al. 2014; Lee et al. 2015). The scatter in the relation is roughly mass-independent, with a value of  $\simeq 0.2 - 0.4$  dex (Behroozi et al. 2013; Speagle et al. 2014), where the exact value depends on e.g. the sample selection method, the SFR indicator(s) used, and the time evolution of the intrinsic relation within the probed redshift range. This relation can be used to define starbursts galaxies as outliers well above this relation (Rodighiero et al. 2011); conversely, galaxies that are well below this relation are referred to as quenched. This relation is also important because its normalisation and scatter may provide important constraints on galaxy formation physics (Torrey et al. 2014; Sparre et al. 2015; Furlong et al. 2015; Mitra et al. 2015; but cf. Kelson 2014).

In the *upper-left panel* of Figure 2, we show the SFR– $M_{*}$  relation for our  $z = 0, 0.2$  and  $0.4$  simulated galaxies selected according to the *sample A* definition in Section 3.3. The points indicate the  $\text{SFR}_{200 \text{ Myr}}$  values of individual galaxies, and the error bars denote the scatter (measured as the 16-84% percentile of the distribution) of the  $\text{SFR}_{10 \text{ Myr}}$  values of the 20 non-overlapping time bins spanning the previous 200 Myr. The normalisation agrees well with compilation of observational constraints (from Behroozi et al. 2013, who compiled the specific SFRs of main sequence galaxies as a function of  $M_{*}$  from various publications; see their Table 5), as already noted by Hopkins et al. (2014). It is clear that some galaxies have very bursty star formation histories because their  $\text{SFR}_{10 \text{ Myr}}$  values can vary by more than an order of magnitude within a 200-Myr period. Another important result is that the 10-Myr SFR variations are much larger in low-mass galaxies ( $M_{*} \lesssim 10^{10} M_{\odot}$ ) than in more-massive galaxies. The *upper-right panel* shows the relation for the  $z = 2$  simulated galaxies. The red triangles (black circles) indicate the median  $\text{SFR}_{200 \text{ Myr}}$  ( $\text{SFR}_{10 \text{ Myr}}$ ) values in different mass bins, and  $\sigma_{\text{MAD}}$  (see definition below) of the  $\text{SFR}_{10 \text{ Myr}}$  and  $\text{SFR}_{200 \text{ Myr}}$  values are denoted by the error bars. The  $\text{SFR}_{10 \text{ Myr}}$  variations are clearly larger than the variations in  $\text{SFR}_{200 \text{ Myr}}$ ; this is a signature of the galaxies’ bursty star formation histories.

The *lower panels* of Figure 2 show that the scatter in the SFR– $M_{*}$  relation. To measure the scatter, we use the standard deviation

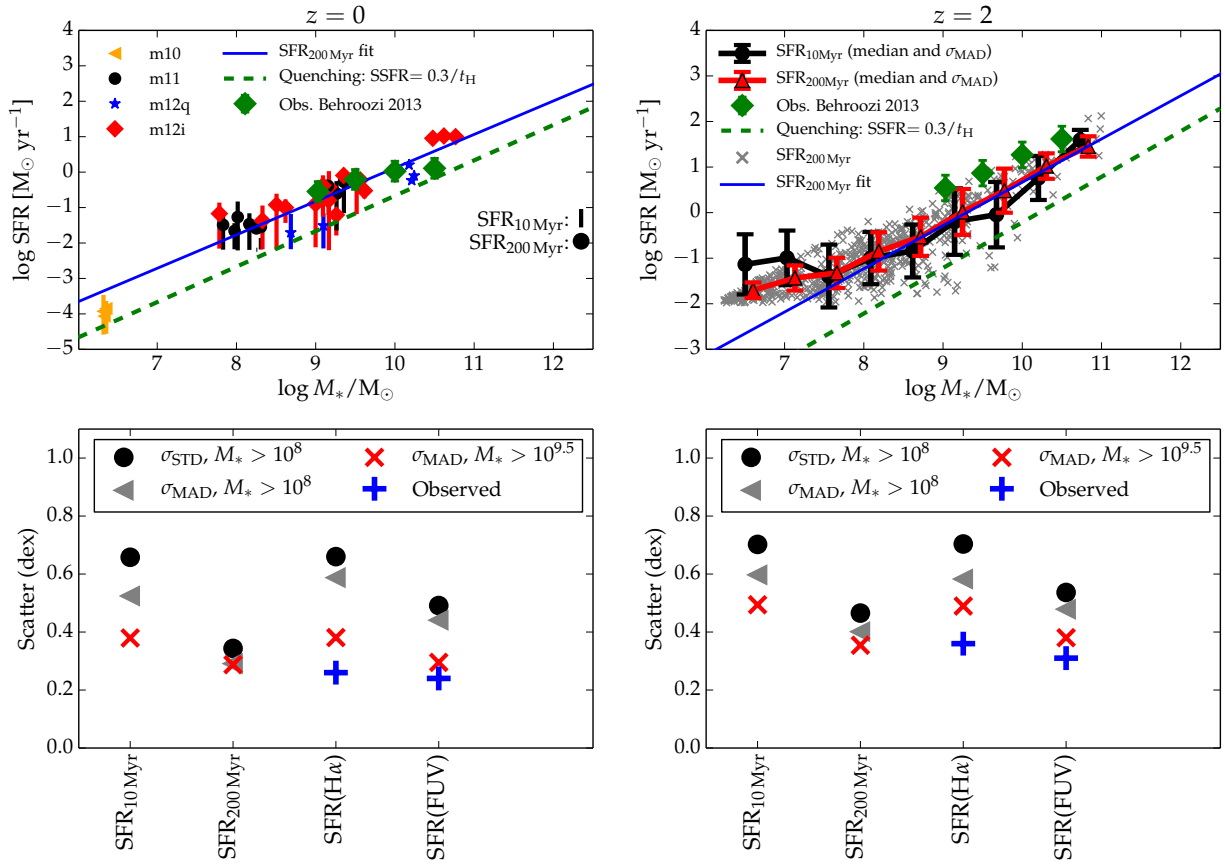


**Figure 2.** *Upper-left panel:* The SFR– $M_*$  relation at  $z = 0, 0.2$  and  $0.4$  measured using the 200-Myr-averaged SFR (different symbols correspond to different simulations, as indicated in the legend). The variability of the 10-Myr-averaged SFR is indicated by the *vertical error bars*, which correspond to the scatter (measured as the 16-84% percentile) of the SFR<sub>10 Myr</sub> values of the 20 non-overlapping time bins spanning the previous 200 Myr. *Upper-right panel:* The median relations for SFR<sub>10 Myr</sub> and SFR<sub>200 Myr</sub> (*circles* and *triangles*, respectively) at  $z = 2$ ; the corresponding errorbars show the scatter (measured as  $\sigma_{\text{MAD}}$ ) in a given mass bin. The *x* symbols in the background show SFR<sub>200 Myr</sub> for individual galaxies. All galaxies have  $\text{SFR} \geq 0.008 M_{\odot} \text{yr}^{-1}$  because our sample only includes galaxies with more than 50 star particles formed in the last 200 Myr (this gives a minimum SFR for the MassiveFIRE galaxies of  $\approx 0.00825 M_{\odot} \text{yr}^{-1}$ ). In the upper panels, the *green dashed lines* indicate the quenching threshold that we use,  $\text{SSFR} < 0.3/t_{\text{H}}$ , where  $t_{\text{H}}$  is the Hubble time at the redshift under consideration. The *green diamonds* show a compilation of observations from Behroozi et al. (2013); the error bars on these points represent the inter-publication variance in the relation, *not the scatter in the relation*. The *blue solid lines* show a fit to the SFR<sub>200 Myr</sub>– $M_*$  relation including all galaxies with  $M_* > 10^8 M_{\odot}$ . *Lower panels:* The scatter in the SFR– $M_*$  relation. For our four different SFR indicators, the scatter is calculated as the standard deviation ( $\sigma_{\text{SD}}$ ) and median absolute deviation ( $\sigma_{\text{MAD}}$ ) of all galaxies with  $M_* > 10^8 M_{\odot}$ . To quantify how the scatter changes when we apply an observationally motivated mass cut of  $M_* > 10^{9.5} M_{\odot}$ , we also show  $\sigma_{\text{MAD}}$  for galaxies with  $M_* > 10^{9.5} M_{\odot}$ . In the  $z = 0$  plot, the *blue + symbols* show the observed scatter in the H $\alpha$ - and FUV-derived relations calculated from the galaxies with  $10^9 < M_*/M_{\odot} < 10^{10}$  from the sample of Weisz et al. (2012). In the  $z = 2$  plot, we show the scatter in the H $\alpha$ - and UV-derived relations from Shivaee et al. (2015). At  $z = 2$ , the normalisation of the simulated galaxies’ relation is slightly lower than the Behroozi et al. (2013) compilation, but recent observations suggest that the observed normalisation may have been overestimated in previous works (see Feldmann et al., in prep. for details). At both redshifts, the scatter in the simulated H $\alpha$ - and UV-derived relations is greater than observed, but the scatter in the simulated galaxies’ relations may not be fully converged (see Section 6), and that in the observed relations may be artificially low because of the methods used to correct for dust attenuation.

(SD) and the median absolute deviation (MAD):

$$\sigma_{\text{SD}} = \sqrt{\frac{1}{N} \sum_i \text{Offset}_i^2},$$

$$\sigma_{\text{MAD}} = 1.4826 \times \text{median}(|\text{Offset}_i - \text{median}[\text{Offset}_i]|).$$

Here,  $\text{Offset}_i$  is the offset in SFR (measured in dex) of a given galaxy from a power-law fit to the SFR– $M_*$  relation.  $i$  is the index of a galaxy, and  $N$  is the total number of galaxies. The factor of 1.4826 in the latter formula makes  $\sigma_{\text{MAD}}$  unbiased relative to  $\sigma_{\text{SD}}$  for a Gaussian distribution. A feature of the MAD is that it is less

sensitive to extreme outliers; thus, starbursts and quenched galaxies do not contribute as much to the MAD as to the SD. We therefore regard  $\sigma_{\text{MAD}}$  as our most reliable estimator of the scatter.

For our four SFR indicators, we calculate the scatter using  $\sigma_{\text{SD}}$  and  $\sigma_{\text{MAD}}$  for all galaxies with  $M_* > 10^8 M_{\odot}$ . Such a mass cut is implemented to eliminate the contribution of very low-mass galaxies, which exhibit very high SFR variability. Of the two estimators,  $\sigma_{\text{MAD}}$  is approximately 0.1 dex smaller than  $\sigma_{\text{SD}}$  for all SFR indicators at both  $z = 0$  and  $z = 2$ , which is expected because the latter estimate is more sensitive to extreme outliers. Real observations of the SFR– $M_*$  relation are only sensitive to a restricted mass range.

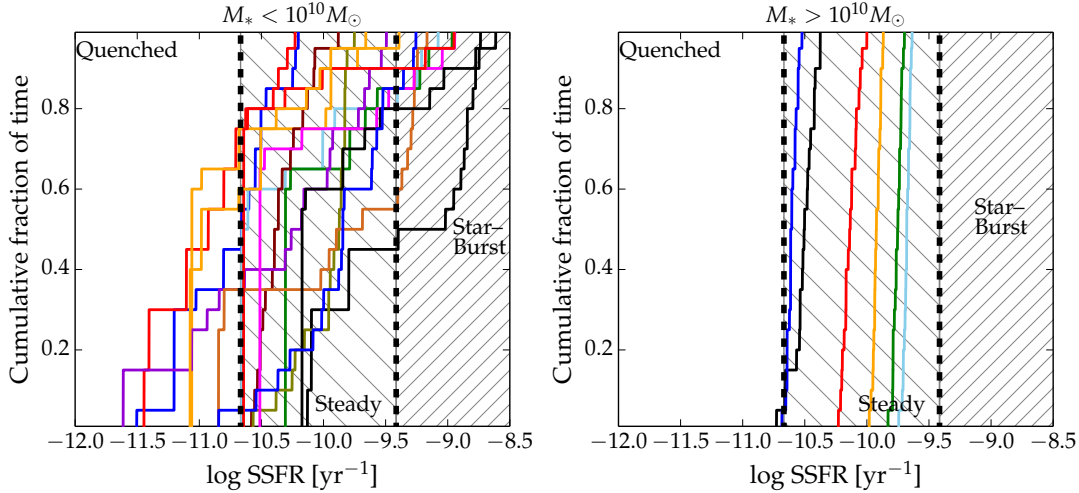


**Figure 3.** Cumulative distribution functions of the 10-Myr-averaged specific SFR,  $\text{SSFR}_{10 \text{ Myr}} \equiv \text{SFR}_{10 \text{ Myr}}/M_*$ , for a subset of the galaxies at  $z = 0, 0.2$  and  $0.4$  in our simulations. The  $\text{SSFR}_{10 \text{ Myr}}$  values were calculated for 20 10-Myr non-overlapping intervals within the last 200 Myr of a galaxy’s history. The dashed vertical lines divide the regions, where a galaxy is classified as quenched (or passive), steady (or ‘main sequence’) and starburst. The *left panel* shows galaxies with  $M_* < 10^{10} M_\odot$ , and the *right panel* shows galaxies with  $M_* > 10^{10} M_\odot$ . In the *left panel*, 15 randomly selected galaxies are shown. At  $z \simeq 0$ , low-mass galaxies have larger SFR fluctuations than more-massive galaxies. In terms of  $\text{SFR}_{10 \text{ Myr}}$ , a low-mass galaxy’s  $\text{SSFR}$  can vary by more than two orders of magnitude within 200 Myr. The galaxies with  $M_* > 10^{10} M_\odot$  are exclusively ‘main sequence’ galaxies.

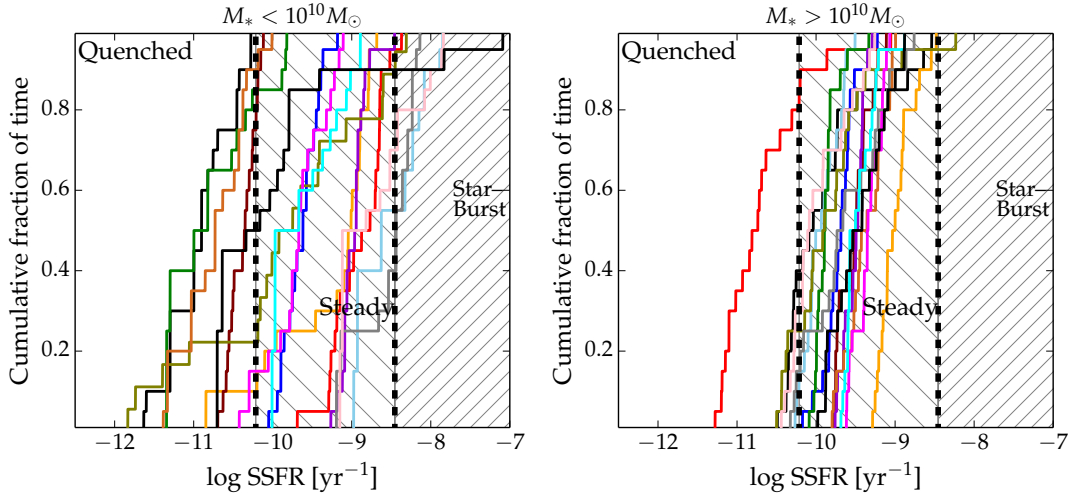


**Figure 4.** Similar to Figure 3, but for  $z = 2$ . Only 15 galaxies are shown in each panel. At this redshift, the high-mass galaxies’  $\text{SSFRs}$  vary more than at  $z = 0$ , but the low-mass galaxies still exhibit greater variations in  $\text{SFR}_{10 \text{ Myr}}$  over 200-Myr intervals.

For example, the  $z = 2$  observations from Shivaei et al. (2015) only include galaxies with  $M_* > 10^{9.5} M_\odot$ . To do a direct comparison with observationally derived values for the scatter, we also calculate  $\sigma_{\text{MAD}}$  using this mass cut.

The scatter is significantly larger for the 10 Myr indicator compared to the 200 Myr indicator: when using  $\text{SFR}_{10 \text{ Myr}}$ , the  $\sigma_{\text{MAD}}$  (for  $M_* > 10^{9.5} M_\odot$ ) is 0.38 dex at  $z = 0$  (0.49 dex at  $z = 2$ ), which is significantly larger than the scatter of 0.29 dex (0.35 dex) obtained with the 200 Myr indicator. Bursty star formation cycles are therefore responsible for the increased scatter in the  $\text{SFR}-M_*$  relation when it is measured with a 10-Myr SFR indicator. When measuring the SFR with a 200-Myr indicator, the signature of the bursty star formation epochs is reduced, and the scatter in the relation is decreased. When comparing  $\sigma_{\text{MAD}}$  obtained with a mass-cut of  $M_* > 10^8 M_\odot$ , the value of the scatter and the difference between the 10 Myr and 200 Myr values are even larger. This

shows that the low-mass galaxies with  $10^8 < M_*/M_\odot < 10^{9.5}$  have a larger amount of SFR-variability than the  $M_* > 10^{9.5} M_\odot$  galaxies.

The result that the scatter in the  $\text{SFR}-M_*$  relation is significantly increased when using a 10-Myr SFR-indicator instead of a 200-Myr indicator shows that the ISM model in the FIRE simulations is more bursty than the widely used sub-resolution physics models (Springel & Hernquist 2003; Oppenheimer & Davé 2006; Scannapieco et al. 2012; Dalla Vecchia & Schaye 2012), which exhibits very little SFR variability on the short timescales that we are considering here (see Figure 5 of Sparre et al. 2015, in which the scatter is almost the same for the instantaneous SFR derived from the gas properties and the 50-Myr-averaged SFR). Even when using  $\text{SFR}_{200 \text{ Myr}}$  as an SFR indicator, there is a significantly larger scatter in the  $\text{SFR}-M_*$  relation in the FIRE simulations compared with the Illustris simulation (Vogelsberger et al. 2013, 2014; Genel

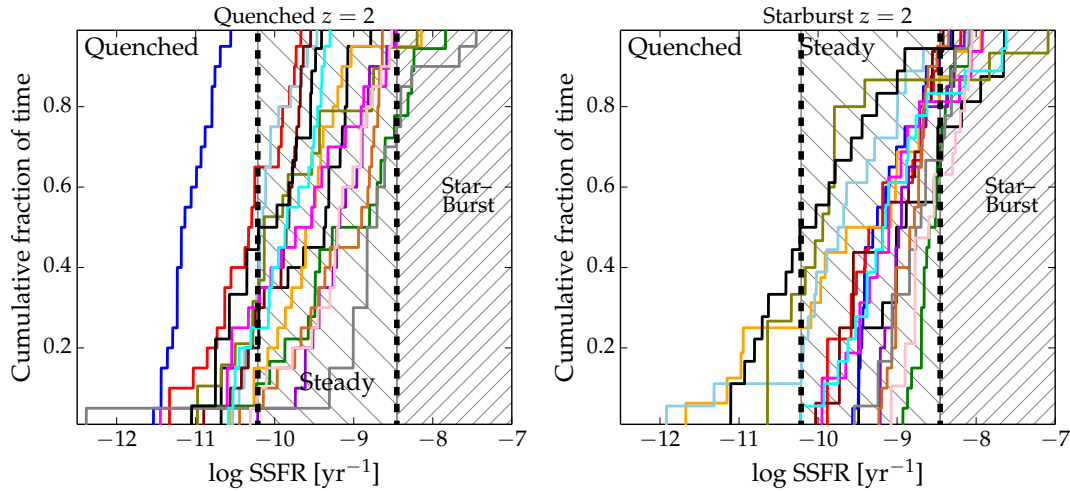


**Figure 5.** The SSFR variability of galaxies at  $z = 2$  selected as being quenched (*left panel*) or starbursts (*right panel*) for at least one of the 20 non-overlapping 10 Myr intervals in the past 200 Myr of their history. Only 15 galaxies are shown in each panel. We again define  $\text{SSFR} \equiv \text{SFR}_{10 \text{ Myr}}/M_*$ . Only one of the ‘quenched’ galaxies is quenched throughout the 200-Myr interval, and four (27 per cent) of the ‘quenched’ galaxies are also classified as starbursts during that interval. Similarly, five (33 per cent) of the ‘starburst’ galaxies are also quenched within 200 Myr. As is shown explicitly below, these results are *not* the consequence of starbursts leading to quenched galaxies but rather high-amplitude SFR variations on short timescales.

et al. 2014). This shows that the FIRE feedback model produces a larger diversity in the galaxy population at a fixed stellar mass compared to the sub-resolution physics model used in Illustris. This result is not surprising because the FIRE star formation and feedback models are designed to resolve several of the star formation processes that occur in GMC-like objects. In contrast, the sub-resolution physics model used in Illustris describes kiloparsec-scale patches of the ISM with an effective equation of state instead of trying to resolve GMC-scale physical processes.

Our estimated scatter at  $z = 2$  according to  $\sigma_{\text{MAD}}$  (for  $M_* > 10^{9.5} M_\odot$ ) is 0.48 dex and 0.37 dex for  $\text{H}\alpha$  and FUV, respectively. The difference between these two values arises because  $\text{H}\alpha$  is more sensitive to short bursts than FUV. The observations at  $z = 2$  show slightly smaller values for the scatter of the two indicators: 0.36 dex and 0.31 dex for  $\text{H}\alpha$  and FUV, respectively. The increased scatter in  $\text{H}\alpha$  compared to UV in these observations could be caused by bursty star formation. However, Shivaei et al. noted that the scatter in the UV-derived relation may be artificially low because the UV slope factors into the SED modelling used to infer  $M_*$ . In contrast, the  $\text{H}\alpha$  fluxes are independently dust-corrected using the Balmer decrement and are not used in the SED modelling. Even though there are systematic uncertainties in observed values of the scatter, the difference between the  $\text{H}\alpha$ -scatter in our simulations and the observations is so large, that it is most likely that the FIRE galaxies are slightly more bursty than observations at  $z = 2$ .

At  $z \simeq 0$  we estimate the observed scatter in the  $\text{SFR}-M_*$  relation by examining the galaxies with  $10^9 < M_*/M_\odot < 10^{10}$  in the sample from Weisz et al. (2012). For  $\text{H}\alpha$  and FUV these galaxies have a scatter of 0.26 dex and 0.24 dex, respectively. This is slightly smaller than what we estimate from our simulations, where we find 0.37 dex and 0.29 dex, respectively. The reason for a larger scatter in the simulations than in the observations is likely that the galaxies in FIRE are slightly more bursty than real galaxies. A feature which is present in both observations and simulations is that the scatter is generally larger at  $z = 2$  than at  $z = 0$ . A plausible explanation for this is smaller SFR-variability at low redshift.

## 4.2 Galaxies going through temporarily quenched and starburst phases

Having studied the  $\text{SFR}-M_*$  relation and its scatter, we will now examine quenched and starburst galaxies. As a definition of a quenched galaxy, we use the criterion  $\text{SSFR} < 0.3/t_{\text{H}}$  (Franx et al. 2008; Williams et al. 2010; Feldmann & Mayer 2015), where  $t_{\text{H}}$  is the Hubble time ( $t_{\text{H}}(z) \equiv 1/H(z)$ , and  $H(z)$  is the Hubble parameter) at the redshift under consideration. This threshold is shown in Figure 2. At  $z = 0$  a starburst galaxy is defined as a galaxy with an SSFR 5.6 times higher than predicted by the observed  $\text{SFR}-M_*$  relation at  $M_* = 10^{10} M_\odot$ . The factor of 5.6 is chosen because it corresponds to a  $2.5\sigma$  outlier above the  $\text{SFR}-M_*$  relation (assuming  $\sigma = 0.3$  dex), and this definition is often used in observational works (e.g. Rodighiero et al. 2011). At  $z = 2$  the normalisation of the  $\text{SFR}-M_*$  relation in our galaxies is 0.6 dex lower than in the compilation of observations from Behroozi et al. (2013), so we here shift the starburst threshold down by this amount. When a galaxy is in between the quenching and starburst thresholds, it is referred to as ‘main sequence’ or *normal* galaxy (e.g. Noeske et al. 2007).

In Figure 3, we show how  $\text{SFR}_{10 \text{ Myr}}/M_*$  of individual galaxies varies over a 200-Myr time interval at  $z = 0$ . Each curve shows the cumulative distribution of the  $\text{SFR}_{10 \text{ Myr}}$  values of a single galaxy calculated in 20 non-overlapping 10-Myr time intervals. The galaxies with  $M_* > 10^{10} M_\odot$  (*right panel*) exhibit a relatively small amount of SFR variability, and individual galaxies’  $\text{SFR}_{10 \text{ Myr}}$  values do not change by more than a factor of three over the 200-Myr interval. Consequently, these galaxies lie on the ‘main sequence’ for the entire 200 Myr. The lower-mass galaxies (*left panel*) exhibit markedly different behaviour: the 10-Myr-averaged SFR can change by more than two orders of magnitude in a 200-Myr time interval, which means that a galaxy can go from being classified as a starburst to a quenched galaxy (in terms of its  $\text{SFR}_{10 \text{ Myr}}$  value) within this time interval. Figure 4 shows the same plots but for  $z = 2$ . As at  $z = 0$ , high-mass galaxies exhibit less  $\text{SFR}_{10 \text{ Myr}}$  variability than do low-mass galaxies. However,  $M_* > 10^{10} M_\odot$  galaxies exhibit more  $\text{SFR}_{10 \text{ Myr}}$  variability at  $z = 2$  than at  $z = 0$ , and unlike at  $z = 0$ , some of the



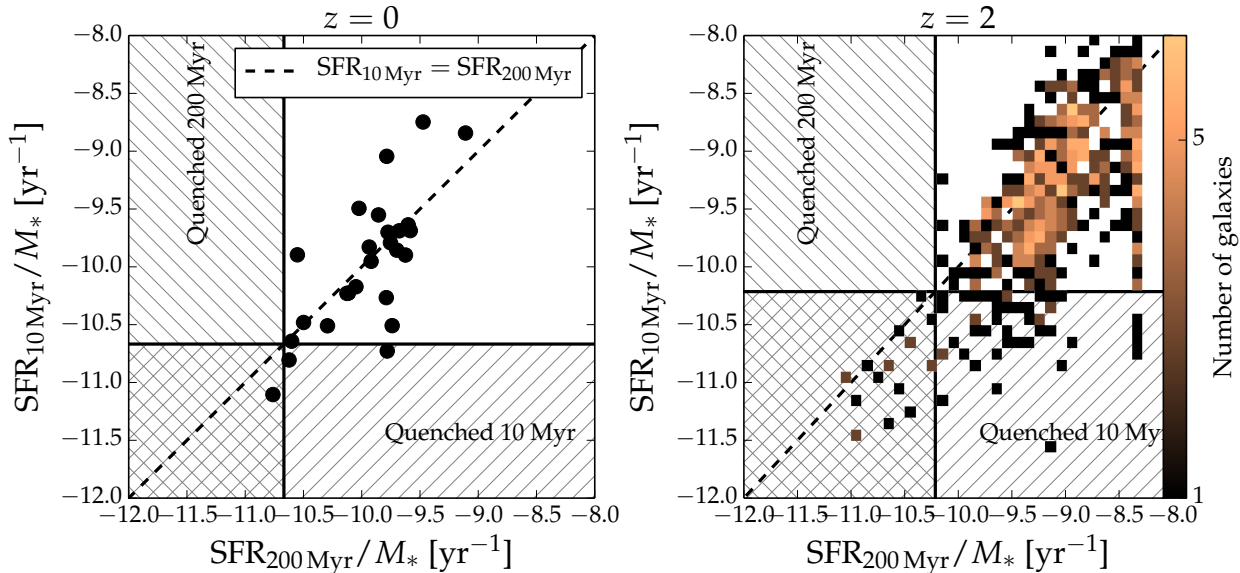


**Figure 6.** Comparison of two measures of the SSFR,  $\text{SFR}_{10 \text{ Myr}}/M_*$  (on the  $y$ -axis) and  $\text{SFR}_{200 \text{ Myr}}/M_*$  (on the  $x$ -axis). The solid horizontal and vertical lines indicate where a galaxy is quenched according to its 10-Myr-averaged SSFR value and 200-Myr-averaged SSFR values, respectively. The *left panel* shows the results for  $z = 0, 0.2$  and  $0.4$ , and the *right panel* shows  $z = 2$ . Most galaxies that are quenched in terms of their 10-Myr-averaged SSFR values (i.e. would be identified as quenched according to  $\text{H}\alpha$  observations) are not quenched in terms of their 200-Myr-averaged SSFR values.

$M_* > 10^{10} M_\odot$  galaxies at  $z = 2$  are classified as both quenched and ‘main sequence’ at different times within a 200 Myr time interval.

Having established that the SFR variability is larger in galaxies with small stellar masses, we will now study samples of galaxies classified as quenched or starbursts in at least one 10 Myr interval within the last 200 Myr before  $z = 2$ . To define such samples, we select galaxies that are obeying the starburst or quenched criteria in at least one 10 Myr interval in the last 200 Myr before  $z = 2$ . Figure 5 shows the  $\text{SFR}_{10 \text{ Myr}}$  distributions for the two samples. For the sample of ‘quenched’ galaxies (*left panel*), the  $\text{SFR}_{10 \text{ Myr}}$  variability is so large that four (27 per cent) of the galaxies are classified as both quenched and starburst galaxies at different times within the 200 Myr. Only one of the 15 galaxies is quenched for the entire 200 Myr. The remaining ten galaxies are on the ‘main sequence’ when they are not quenched. For the sample of starburst galaxies (*right panel*), there are similar large  $\text{SFR}_{10 \text{ Myr}}$  fluctuations. The starbursts lie on the ‘main sequence’ for most ( $\gtrsim 60$  per cent) of the 200-Myr time interval, and five of the starburst galaxies are also classified as quenched during the 200-Myr period. We note that the starbursts are *not* driven by major mergers but rather by internal processes (see Section 6). Consequently, a galaxy being above the ‘main sequence’ is insufficient evidence to claim that it is undergoing a major merger.

Note that we have based our quenching and starburst definitions on the 10-Myr-averaged SFR. The galaxies quenched according to this definition are most likely not permanently quenched; instead, they are going through a temporarily quenched phase.

### 4.3 The fractions of quenched and starburst galaxies according to different SFR indicators

The population of quenched galaxies depends on the quenching criterion employed. In particular, for quenched definitions based on the specific SFR ( $\text{SSFR} \equiv \text{SFR}/M_*$ ), the timescale of the SFR indicator used is important. Figure 6 shows  $\text{SSFR}_{10 \text{ Myr}} \equiv$

$\text{SFR}_{10 \text{ Myr}}/M_*$  versus  $\text{SSFR}_{200 \text{ Myr}} \equiv \text{SFR}_{200 \text{ Myr}}/M_*$  for the  $z = 0$  (*left*) and  $z = 2$  (*right*) galaxies. The galaxies are selected according to the *sample A* criterion in Section 3.3, which biases towards less quenching. The vertical and horizontal lines denote the quenching threshold,  $\text{SSFR} < 0.3/t_{\text{H}}$ . Galaxies below (to the left of) these lines are classified as quenched in terms of their  $\text{SSFR}_{10 \text{ Myr}}$  ( $\text{SSFR}_{200 \text{ Myr}}$ ) values. Galaxies in the lower-left quadrant are quenched in terms of both their  $\text{SSFR}_{200 \text{ Myr}}$  and  $\text{SSFR}_{10 \text{ Myr}}$  values.

All galaxies that satisfy the  $\text{SSFR}_{200 \text{ Myr}}$  quenched criterion also satisfy the  $\text{SSFR}_{10 \text{ Myr}}$  quenched criterion. In contrast, the majority of galaxies that are quenched in terms of their  $\text{SSFR}_{10 \text{ Myr}}$  values are *not* quenched in terms of  $\text{SSFR}_{200 \text{ Myr}}$ . Consequently, if observed with a short-timescale SFR tracer (e.g.  $\text{H}\alpha$ ), they would be considered quenched; however, if they were observed with a longer-timescale SFR tracer (e.g. UV or far-infrared), they would not be. Even when a galaxy is quenched in terms of  $\text{SSFR}_{200 \text{ Myr}}$ , because UV and infrared emission can be ‘contaminated’ by intermediate-age stellar populations (Hayward et al. 2014b; Utomo et al. 2014), it may not be identified as quenched. Moreover, galaxies may be temporarily quenched for hundreds of Myr because of the gusty nature of stellar feedback-driven outflows (Muratov et al. 2015). It is thus (perhaps surprisingly) quite difficult to judge whether a galaxy is permanently quenched based on observational measures of its SFR. Galaxy colors are a more robust measure of whether a galaxy is quenched, but it is necessary for a galaxy’s star formation to have been quenched for  $\gtrsim 0.5$  Gyr for it to proceed through the post-starburst phase and onto the red sequence (e.g. Snyder et al. 2011; Hayward & Smith 2015). Moreover, one must still worry about the effects of dust, which can make an actively star-forming galaxy appear quenched.

The galaxies that are quenched in terms of  $\text{SSFR}_{10 \text{ Myr}}$  but not  $\text{SSFR}_{200 \text{ Myr}}$  are mainly low-mass galaxies that are ‘observed’ shortly after a burst. As noted in Section 4.2, the SFRs of low-mass galaxies can vary by greater than two orders of magnitude within 200 Myr. At  $z = 2$ , even massive ( $M_* > 10^{10} M_\odot$ ) galaxies can

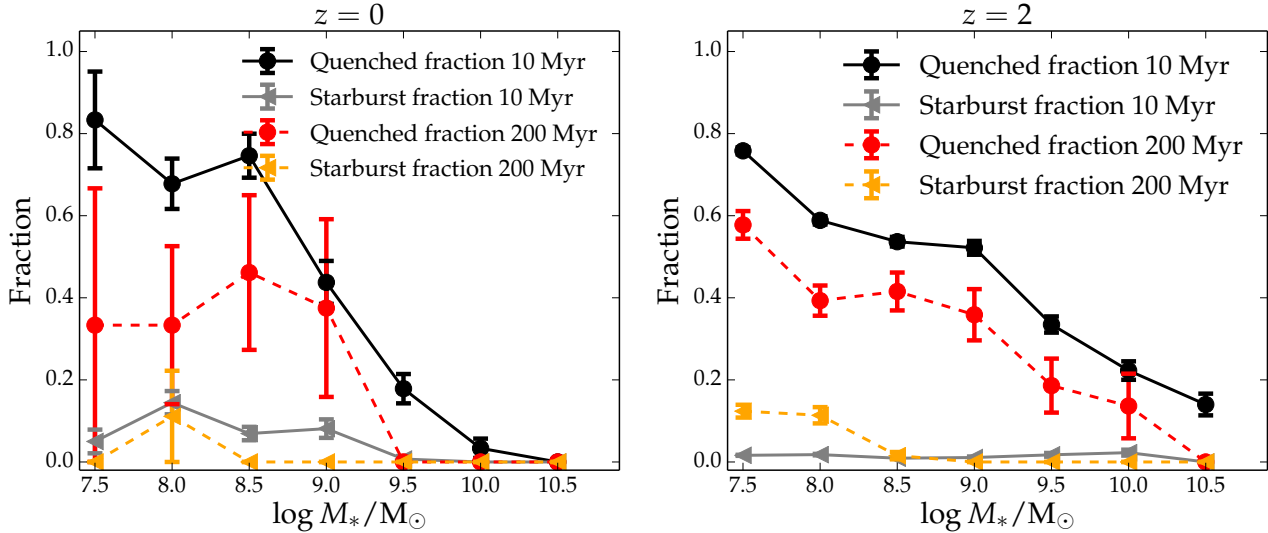


**Figure 7.** The fractions of quenched galaxies and starbursts according to the 10-Myr and 200-Myr averaged SFRs versus stellar mass; the *left* panel shows the results for  $z = 0, 0.2$  and  $0.4$ , and the *right* shows  $z = 2$ . At  $z = 0$ , in terms of  $\text{SFR}_{10 \text{ Myr}}$ , the quenched fraction can be as high as 80 per cent, whereas it is slightly smaller when  $\text{SFR}_{200 \text{ Myr}}$  is used. The starburst fraction can be as high as  $\simeq 15$  per cent when  $\text{SFR}_{10 \text{ Myr}}$  is used, and it decreases with stellar mass. When  $\text{SFR}_{200 \text{ Myr}}$  is used, the starburst fraction is zero except for in the low-mass bins. At  $z = 2$ , greater fractions of galaxies are quenched at most masses in terms of both  $\text{SFR}_{10 \text{ Myr}}$  and  $\text{SFR}_{200 \text{ Myr}}$  because of the higher SFR variability at this redshift.

be classified as both quenched and ‘main sequence’ within 200 Myr according to their  $\text{SSFR}_{10 \text{ Myr}}$  values (Figure 4). Thus, at  $z \simeq 2$ , galaxies may be mistaken as quenching or quenched galaxies when in reality, they will be forming stars again with a high SSFR within 100 Myr. Barro et al. (2015) presented observations of GDN-8231, a  $M_* = 10^{10.75} M_\odot$  galaxy at  $z = 1.674$  with a young stellar population with an age of 750 Myr and  $\text{H}\alpha$ - and  $24\text{-}\mu\text{m}$ -derived SFRs of  $\lesssim 10 M_\odot \text{yr}^{-1}$ . They interpreted these observations as evidence that the galaxy is ‘caught in the act’ of quenching. However, both  $\text{H}\alpha$ - and  $24\text{-}\mu\text{m}$  emission are short-timescale SFR indicators. The right panel of Figure 4 indicates that in terms of  $\text{SSFR}_{10 \text{ Myr}}$ , even massive galaxies at  $z = 2$  may be classified as both quenched and normal star-forming galaxies within 200 Myr. Thus, perhaps GDN-8231 has been observed in a temporary phase of low  $\text{SSFR}_{10 \text{ Myr}}$  and is not in fact permanently quenched.

To further assess the frequencies of quenched and starburst galaxies, we plot their fractions versus stellar mass at  $z = 0$  and  $z = 2$  in Figure 7. We include all the galaxies in sample B from section 3.3. Both the quenched and starburst galaxy fractions are calculated using both  $\text{SFR}_{10 \text{ Myr}}$  and  $\text{SFR}_{200 \text{ Myr}}$  (and the same definitions as in Section 4.2). For the fractions based on  $\text{SFR}_{10 \text{ Myr}}$ , we include one value for each of the 20 non-overlapping 10-Myr intervals within the last 200 Myr. At  $z = 0$  (*left panel*), when  $\text{SFR}_{10 \text{ Myr}}$  is used, the quenched fraction can be as high as 80 per cent, whereas it is slightly smaller for  $\text{SFR}_{200 \text{ Myr}}$ . The starburst fraction can be as high as  $\simeq 15$  per cent when  $\text{SFR}_{10 \text{ Myr}}$  is used, whereas it is zero for all but the  $M_* = 10^8 M_\odot$  bin when  $\text{SFR}_{200 \text{ Myr}}$  is used. Both the starburst and quenched galaxy fractions decrease with stellar mass because at  $z = 0$ , the high-mass galaxies have relatively constant SSFRs (see the right panel of Figure 3). At  $z = 2$  (*right panel*), greater fractions of galaxies are quenched at high masses in terms of both  $\text{SFR}_{10 \text{ Myr}}$  and  $\text{SFR}_{200 \text{ Myr}}$  because of the more gradually declining SFR variability at this redshift (compare Figures 3 and 4). The fraction of starbursts is 1–3% for  $10^9 M_\odot < M_* < 10^{10.5} M_\odot$ , which is consistent with the fraction of 2% observed by Rodighiero et al. (2011) for galaxies

with  $M_* > 10^{10} M_\odot$  at  $z = 2$ . Interestingly, for the two lowest-mass bins, the starburst fraction is higher when  $\text{SFR}_{200 \text{ Myr}}$  is used than when  $\text{SFR}_{10 \text{ Myr}}$  is used. The reason for this perhaps counter-intuitive result is that for these low-mass galaxies,  $\text{SFR}_{200 \text{ Myr}}$  can be sufficiently elevated by a single  $< 10\text{-Myr}$  burst to make the galaxy classified as a starburst. Such a galaxy would be a starburst according to  $\text{SFR}_{10 \text{ Myr}}$  for only one 10-Myr interval. A population composed exclusively of such galaxies would have starburst fractions of 1 and 0.05 according to  $\text{SFR}_{200 \text{ Myr}}$  and  $\text{SFR}_{10 \text{ Myr}}$ , respectively.

The quenched fractions shown in Figure 7 should not be haphazardly compared with observations because many of the galaxies that are quenched even according to  $\text{SFR}_{200 \text{ Myr}}$  are only quenched temporarily. Thus, one must compare the results presented here with quenched fractions inferred from observations in a compatible manner. A more observationally motivated comparison can for example be based on the  $\text{H}\alpha$  equivalent width, which is an approximate measure of the SSFR (Fumagalli et al. 2012). This measure indicates some tension between the fraction of central galaxies in our simulations that are quenched and the observations of Geha et al. (2012), who demonstrated that in SDSS, no field galaxies at  $z = 0$  with  $M_* < 10^9 M_\odot$  have  $\text{H}\alpha$  equivalent widths of less than  $2 \text{ \AA}$ . In our simulations, 3 out of 10 central galaxies (30 per cent) from our sample B at  $z = 0$  with  $10^8 < M_*/M_\odot < 10^9$  have equivalent widths<sup>4</sup> of less than  $2 \text{ \AA}$ . At  $z = 2$ , a similar fraction of 39 out of 135 (29 per cent) is found. Even though only a minority of galaxies have equivalent widths smaller than  $2 \text{ \AA}$ , the fraction is larger than the 0% observed by Geha et al. (2012). Thus, observed  $\text{H}\alpha$  equivalent width distributions provide important constraints on the fraction of galaxies being quenched according to a  $\simeq 10\text{-Myr}$  SFR indicator. However, we note that despite the very high resolution of these simulations, it is possible that this apparent tension

<sup>4</sup> We have here calculated the  $\text{H}\alpha$  equivalent width from the nebular flux and the stellar continuum in the WFC3 UVIS F657N filter using the SLUG code.

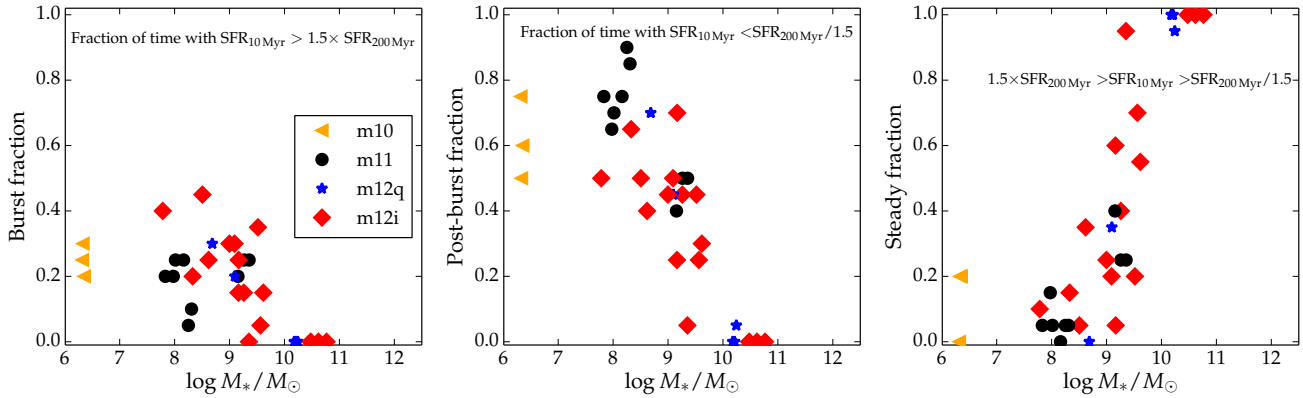


**Figure 8.** For each galaxy at  $z = 0, 0.2$  and  $0.4$ , we show the fraction of time within the last 200 Myr that the galaxy has spent in burst (with  $\text{SFR}_{10\text{Myr}} > 1.5 \times \text{SFR}_{200\text{Myr}}$ ), post-burst (with  $1.5 \times \text{SFR}_{10\text{Myr}} < \text{SFR}_{200\text{Myr}}$ ), and steady star-forming phases. Galaxies with  $M_* > 10^{10} M_\odot$  spend most of their time forming stars steadily, whereas galaxies with lower masses spend a significant fraction of their time in burst and post-burst phases.

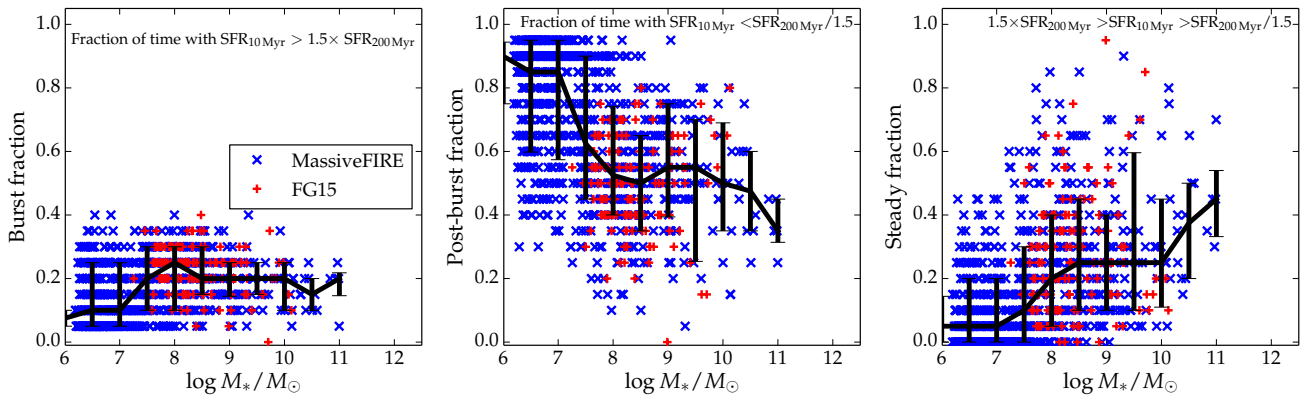


**Figure 9.** Similar to Figure 8, but for  $z = 2$ . The 16–84th percentile ranges for different stellar mass bins are also shown (*black error bars*), and the median relation is shown as a black line. In contrast with  $z = 0$ , galaxies of all masses spend  $\simeq 20$  per cent of the time in bursts. The fraction of time spent in steady (post-burst) phases increases (decreases) with stellar mass.

is an artefact of not resolving sufficiently far down the GMC mass function; we discuss this in detail in Section 6.

## 5 CHARACTERISATION OF INDIVIDUAL BURSTY STAR FORMATION HISTORIES

In the previous section, we focused on how the burstiness of the FIRE galaxies’ SFHs affects population-based measures such as the  $\text{SFR}-M_*$  relation and fractions of quenched and starburst galaxies. We now analyze the detailed star formation histories of individual galaxies. All the analysis in this section is based on galaxies selected to have well-sampled star formation histories according to the *sample A* definition in Section 3.3.

### 5.1 Dividing a star formation history into post-burst, steady and burst phases

The terms post-burst and burst refer to a galaxy’s current star-formation rate being lower and higher, respectively, than some measure of its SFR in the recent past. In this section, we choose a definition of burstiness that quantifies how actively star-forming a galaxy has been in the last 10 Myr of its lifetime compared to the last 200

Myr. Specifically, we define a galaxy to be in burst, post-burst or steady phases based on the following criteria:

Burst phase:  $\text{SFR}_{10\text{Myr}} > 1.5 \times \text{SFR}_{200\text{Myr}}$ ,

Post-burst phase:  $\text{SFR}_{10\text{Myr}} < \frac{\text{SFR}_{200\text{Myr}}}{1.5}$ ,

Steady phase:  $\frac{\text{SFR}_{200\text{Myr}}}{1.5} < \text{SFR}_{10\text{Myr}} < 1.5 \times \text{SFR}_{200\text{Myr}}$ .

The factors of 1.5 in these definitions are arbitrary. In observational applications, one approach would be to study the statistical behaviour of  $\text{SFR}(\text{H}\alpha)/\text{SFR}(\text{FUV})$ , which characterises whether a galaxy is undergoing a burst (see Section 2) for a large sample of galaxies and consequently infer the roles of the burst, post-burst and steady phases of star formation histories. Another approach is to use a combination of the 4000-Å break and the Balmer absorption-line index  $\text{H}\delta_A$  to constrain the mass fraction formed in a recent burst (Kauffmann et al. 2003). However, the focus of the current analysis is to theoretically illustrate how stars are formed in simulations, which is clearer if we use the above definitions. In Section 5.3, we will provide a direct comparison with observations in terms of the  $\text{SFR}(\text{H}\alpha)/\text{SFR}(\text{FUV})$  ratio.

The *left panel* of Figure 8 shows the fraction of time that

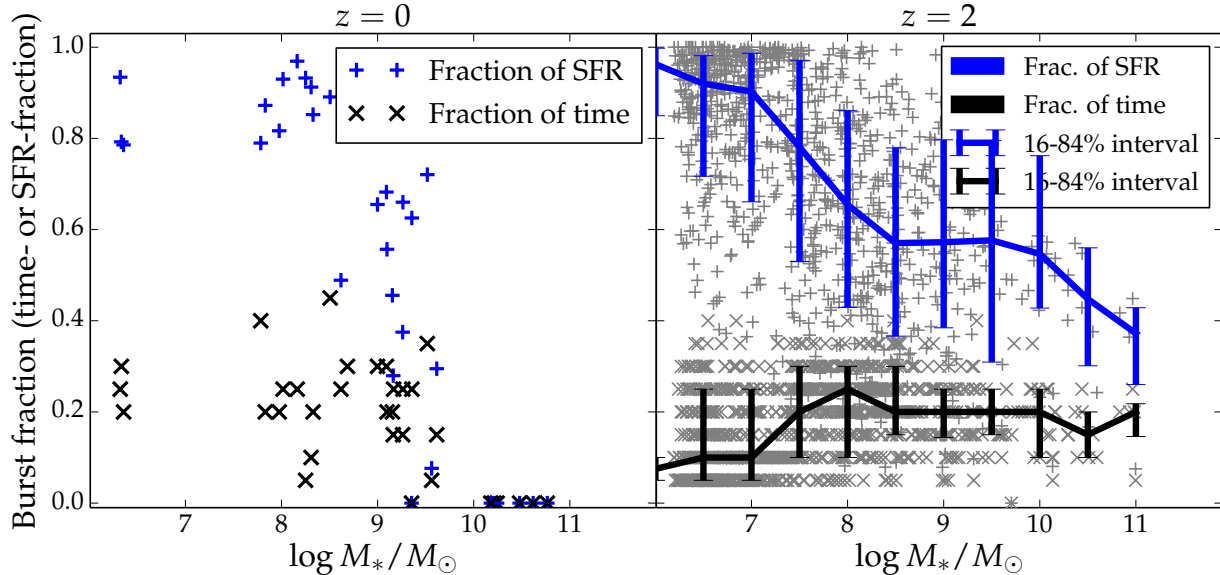


**Figure 10.** The fraction of time spent ( $x$  symbols) and the fraction of stellar mass formed ( $+$  symbols) in burst cycles. Again, a galaxy is defined to be in a burst phase when  $\text{SFR}_{10 \text{ Myr}} > 1.5 \times \text{SFR}_{200 \text{ Myr}}$ . The *left* panel shows galaxies at  $z = 0, 0.2$  and  $0.4$ , and the *right* panel shows  $z = 2$  galaxies. For the  $z = 2$  galaxies, the 16–84th percentile ranges are indicated by the error bars. At  $z = 0$ , galaxies with  $M_* \lesssim 10^9 M_\odot$  spend  $\simeq 25\%$  of their time and form  $\simeq 80\%$  of their stars in burst cycles. More-massive galaxies are not bursty. At  $z = 2$ , the fraction of time spent in bursts (the *duty cycle*) is  $\simeq 20\%$ , independent of the galaxy mass. The fraction of the stellar mass formed in bursts decreases from  $\simeq 100\%$  at the lowest masses to  $\simeq 40\%$  at  $M_* = 10^{11} M_\odot$ .

galaxies at  $z = 0$  have spent in burst phases over the previous 200 Myr<sup>5</sup>. Low-mass galaxies ( $M_* \lesssim 10^9 M_\odot$ ) typically form stars in burst phases for 20–40% of the time, whereas more-massive galaxies form fewer stars in bursts. All of the  $z = 0$  galaxies with  $M_* > 10^{10} M_\odot$  have not had any bursts within the past 200 Myr. The *central panel* shows that low-mass galaxies are typically in post-burst phases 50–80% of the time. The interpretation is that if a galaxy forms stars in sufficiently intense burst cycles, the galaxy is classified as post-burst for a large fraction of the time (according to the criteria formed above but not necessarily observational indicators of post-starburst galaxies; see Snyder et al. 2011 for a detailed study of the latter). Galaxies with  $M_* > 10^{10} M_\odot$  are never in a post-burst phase during the 200 Myr before  $z = 0$ . The *right panel* shows the fraction of time for which a galaxy is classified as steady. At  $z = 0$ , the  $M_* > 10^{10} M_\odot$  galaxies are always in a steady phase, whereas galaxies with  $M_* \lesssim 10^9 M_\odot$  spend  $\lesssim 20$  per cent of the time in steady phases.

Figure 9 shows the analogous plots for  $z = 2$ . In these plots, we also show the median values (connected with black lines) and 16–84th percentile ranges (error bars) in various mass bins. Similar trends are observed for the mass-dependence of the post-burst and steady fractions, but the mass-dependence of the burst fraction is less pronounced than at  $z = 0$ . This result indicates that massive galaxies form stars in a more bursty manner at  $z = 2$  than at  $z = 0$ , presumably because they exhibit violent outflows and subsequent cessation of star formation at  $z = 2$  but not  $z = 0$  (Muratov et al. 2015).

Given the large amplitudes and frequency of the starbursts experienced by the FIRE galaxies, it is worth considering how much

stellar mass is formed in bursts. Figure 10 shows the fraction of stars formed (blue crosses) and time spent (black  $\times$ 's) in burst phases for  $z = 0$  (*left*) and  $z = 2$  (*right*). At  $z = 0$ , low-mass galaxies ( $M_* < 10^9 M_\odot$ ) form most of their stars ( $\gtrsim 80\%$ ) in bursts, but they spend a relatively small fraction of their time (15–35%) in burst phases. As expected from the above discussion, both fractions are zero for galaxies with  $M_* > 10^{10} M_\odot$ . At  $z = 2$ , the lowest-mass galaxies form effectively all of their stars in bursts despite spending  $\lesssim 20\%$  of their time in bursts; the reason is that most of their time is spent in post-burst phases (see Figure 8), in which their SFRs are extremely low. Although massive galaxies spend a similar (or even slightly greater) fraction of the time in bursts, the fractions of their stars formed in bursts are less than for low-mass galaxies ( $\lesssim 50\%$  for the most-massive galaxies) because the massive galaxies spend a large fraction of their time in steady phases, in which the SFRs are less than in the burst phases but still sufficiently high to account for a significant fraction of the stellar mass formed over the 200-Myr interval. Still, the fact that massive galaxies at  $z = 2$  form approximately half of their stars in bursts is in marked contrast with  $z = 0$ , where massive galaxies form effectively no stars in bursts.

## 5.2 The variability timescale and duration of burst cycles

Until now, we have studied the SFR variability on timescales equal to or longer than 10 Myr, which is the regime in which the SFR can be constrained by observations. Despite being observationally inaccessible, variability on shorter timescales might play an important role in shaping galaxies and is thus worthy of analysis. To examine the SFR variability on small timescales, in Figure 11, we plot the SFR in bins of width 1 Myr for 25 randomly chosen galaxies with  $M_* < 10^{10} M_\odot$  from the MassiveFIRE suite (galaxies more massive than  $M_* = 10^{10} M_\odot$  are discussed in Feldmann et al., in prep.). To obtain well-sampled star formation histories, we select galaxies that have formed more than 5000 star particles over

<sup>5</sup> In Figure 8,  $\text{SFR}_{200 \text{ Myr}}$  is calculated at  $z = 0$ , and  $\text{SFR}_{10 \text{ Myr}}$  is calculated in 20 non-overlapping time bins of lookback times between 0 and 200 Myr. We also calculated  $\text{SFR}_{200 \text{ Myr}}$  in running time bins starting at the same lookback time as each of the  $\text{SFR}_{10 \text{ Myr}}$ -intervals, and this did not change our results.

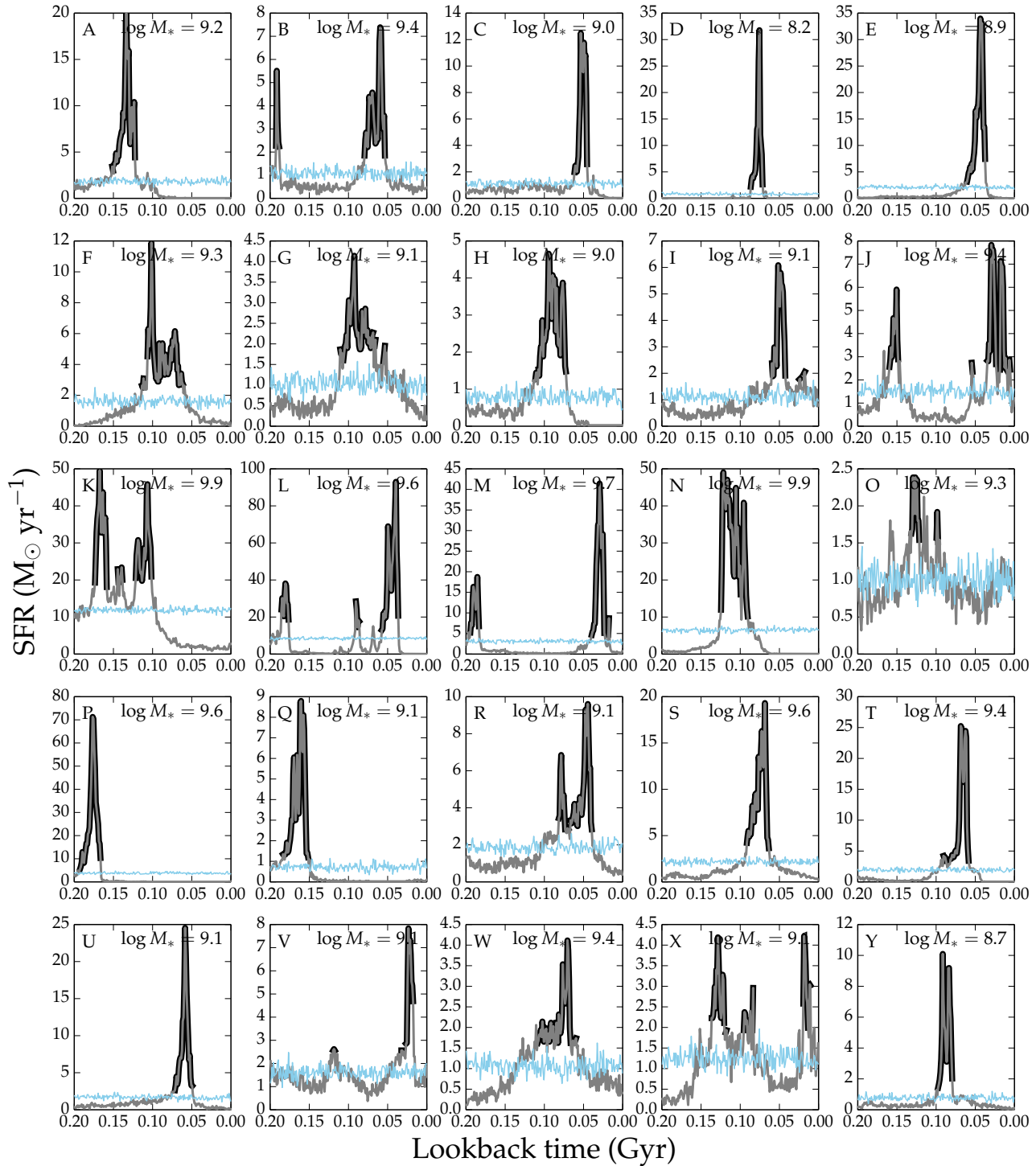


**Figure 11.** Each panel shows the last 200 Myr of the star formation history of a galaxy at  $z = 2$  (grey line) binned in 1-Myr time bins. A galaxy is defined to be in a burst phase (marked by thick black lines), when the SFR is greater than 1.5 times the average SFR over the last 200 Myr of a galaxy’s lifetime. An example of how the SFH would look if all of the variability were due to Poisson noise of the sampling of star particles is shown by the thin blue line. The stellar masses in solar units are shown in the upper right corners. The figure shows that the shortest bursts in the FIRE simulations have durations of 5-50 Myr, and the SFR peaks typically have durations of at least 3 Myr.

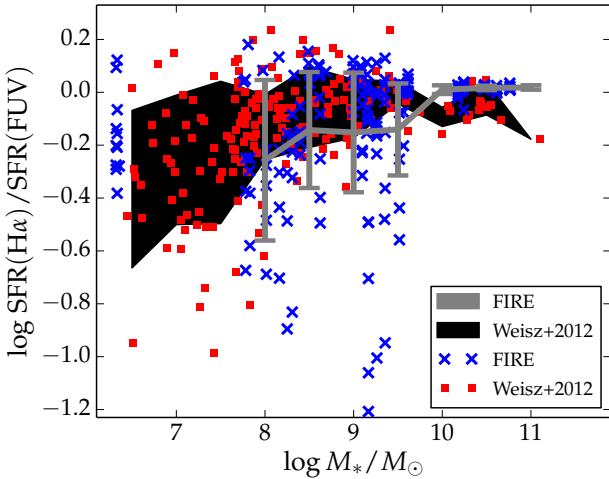


**Figure 12.**  $\text{SFR}(\text{H}\alpha)/\text{SFR}(\text{FUV})$  versus stellar mass for the simulated galaxies in FIRE at  $z = 0, 0.2$ , and  $0.4$  (blue  $\times$  symbols). For each galaxy at these redshifts, we show the  $\text{SFR}(\text{H}\alpha)/\text{SFR}(\text{FUV})$  ratio at look-back times of 0, 25, 50, 75 and 100 Myr. The grey line with error bars indicates the median values and 16–84th percentile ranges for different mass bins. Data for local galaxies from Weisz et al. (2012) are shown as red squares, and the 16–84th percentile ranges for different mass bins are indicated by the black contour. The scatter in the  $\text{SFR}(\text{H}\alpha)/\text{SFR}(\text{FUV})$  values is a measure of the burstiness of the star formation histories. The  $\text{SFR}(\text{H}\alpha)/\text{SFR}(\text{FUV})$  ratios of the galaxies in the FIRE simulations are broadly consistent with the observational data except that in the mass range of  $10^8 - 10^{9.5} M_{\odot}$ , there is a population of simulated galaxies with significantly lower  $\text{SFR}(\text{H}\alpha)/\text{SFR}(\text{FUV})$  ratios than observed; this may be caused by the GMC mass function not being resolved to sufficiently low masses in the simulations.

the last 200 Myr within 20% of the virial radius of the halo. This corresponds to the requirement that  $\text{SFR}_{200 \text{ Myr}} \gtrsim 1 M_{*} \text{ yr}^{-1}$ . We mark galaxies as being in a burst phase (thick black lines) when the SFR is at least 1.5 times the  $\text{SFR}_{200 \text{ Myr}}$  value at  $z = 2$ . Some of the shortest bursts are shown in panels D, E, P and U, where the SFR exhibits a single peak, and before (after) the peak the SFR increases (decreases) monotonically. In all of these cases, the burst peak is resolved by at least three time bins, which implies that the shortest variability timescales of bursts are of order 3 Myr. The most common type of bursts have longer durations and more complex shapes; see e.g. panels F, G, N and W. The typical bursts duration in these panels are 25–100 Myr, but some short spikes have durations as short as 3–5 Myr.

The presence of SFR variability on timescales as small as 3 Myr suggests that the FIRE feedback model leads to SFR fluctuations that cannot be probed using standard SFR indicators such as  $\text{H}\alpha$  and FUV emission.<sup>6</sup> An important consequence of such fast SFR variability is related to the inner density profiles of dark matter halos because SFR variability on timescales less than the local orbital period of dark matter particles can turn dark matter cusps into cores (Pontzen & Governato 2012).

<sup>6</sup> In principle, these fluctuations could be probed for local galaxies by analysing their resolved stellar populations (for recent examples of such analyses, see e.g. Weisz et al. 2008, 2011, 2014; Johnson et al. 2013; Williams et al. 2015).

### 5.3 Comparing with observations of local galaxies

To directly compare the SFR variability of the FIRE galaxies with observations, we now consider the ratio of the  $\text{H}\alpha$ -derived SFR to the FUV-derived SFR,  $\text{SFR}(\text{H}\alpha)/\text{SFR}(\text{FUV})$ . This ratio is a sensitive probe of the SFR variability of *individual galaxies*, in contrast with e.g. comparisons of the scatter in the  $\text{SFR}-M_{*}$  relations obtained using different SFR indicators, because it quantifies the difference between the SFR indicators for the same galaxy. Figure 12 compares the  $\text{H}\alpha$  to FUV ratios of 185 local galaxies from Weisz et al. (2012) with those of the  $z = 0$  FIRE galaxies (see Section 2.1 for details regarding how the ratios are calculated for the simulations). The individual observational (simulation) data points are denoted with *red squares* (*blue  $\times$ 's*), and the 16–84th percentile ranges for different mass bins are denoted by the *black contour* (*grey error bars*).

The median value of  $\text{SFR}(\text{H}\alpha)/\text{SFR}(\text{FUV})$  at high masses is  $\simeq 1$  for both the observed and simulated galaxies. The ratio decreases with decreasing stellar mass: at  $M_{*} \simeq 10^8 M_{\odot}$ , the median value is  $\simeq 0.6$ . This suppressed  $\text{H}\alpha/\text{FUV}$  ratio is potentially a signature of bursty star formation being common in real low-mass galaxies (e.g. Lee et al. 2009; Weisz et al. 2012), and in the simulations, it is definitely a consequence of the rapid SFR variability exhibited by low-mass galaxies (because other possible factors, chiefly incomplete sampling of the IMF and differential dust attenuation, are not modelled). As demonstrated in Section 2, strong bursts with durations of order 10 Myr can cause the  $\text{SFR}(\text{H}\alpha)/\text{SFR}(\text{FUV})$  ratio to be systematically less than 1 (see Weisz et al. 2012 for a more detailed analysis).

Regarding the scatter, at high masses ( $M_{*} > 10^{10} M_{\odot}$ ), the scatter in the FIRE simulations'  $\text{SFR}(\text{H}\alpha)/\text{SFR}(\text{FUV})$  ratios is less than the observed scatter. The scatter appears to be less in the simulations, but this may be an artifact of the small number of massive galaxies at  $z = 0$ . The scatter in the ratio increases with decreasing stellar mass for both the observations and simulations. At lower masses,  $M_{*} \lesssim 10^{9.5} M_{\odot}$ , the scatter is larger than in the more-massive galaxies for both the simulations and the observations. A difference between the observations and simulations is that the scatter is slightly larger at low masses in the simulations compared to the observations.

Overall, the majority of galaxies have  $\text{SFR}(\text{H}\alpha)/\text{SFR}(\text{FUV})$  ratios consistent with observations, but a fraction of galaxies do, however, have significantly lower ratios than observed. This makes the scatter in  $\text{SFR}(\text{H}\alpha)/\text{SFR}(\text{FUV})$  of the simulated galaxies around 0.2 dex larger than the observations for  $M_{*} \lesssim 10^{9.5} M_{\odot}$ . This is a sign that the population of simulated galaxies is slightly more bursty than real galaxies. This confirms the result from Section 4.1, where the scatter of the  $\text{SFR}-M_{*}$  relation was found to be slightly larger than in observations. Even though the FIRE galaxies seem to become bursty at a slightly larger  $M_{*}$  value than the observed sample of galaxies, we find it encouraging that the burstiness of the simulated galaxies' star formation histories decreases with increasing stellar mass, consistent with observations.

### 5.4 Convergence studies

When analysing the  $\text{H}\alpha/\text{FUV}$  ratio, it is crucial to be aware of how well-converged the strength and duration of burst cycles are. To analyse how the signature of burst cycles changes with resolution, we compare  $\text{SFR}(\text{H}\alpha)/\text{SFR}(\text{FUV})$  of the high-resolution (HR) and standard-resolution (SR) versions of the MassiveFIRE simulations at  $z = 2$  in Figure 13. In this figure, open symbols indicates galax-

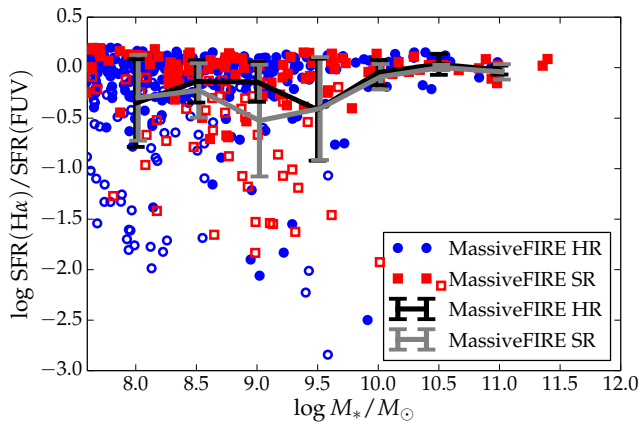


**Figure 13.** The high-resolution (HR) MassiveFIRE runs are compared to the standard-resolution (SR) runs. Open symbols show galaxies in which no stars are formed in the last 10 Myr before  $z = 2$ ; for such galaxies, the SFR is set to a resolution-dependent upper limit (see text for details). For most mass ranges, there is good agreement between the 16-84% percentiles of  $\text{SFR}(\text{H}\alpha)/\text{SFR}(\text{FUV})$  for the HR and the SR simulations. One difference is present at  $M_* = 10^9 M_\odot$ , where the SR runs show a larger scatter because a large fraction of galaxies have formed no stars in the last 10 Myr before  $z = 2$ , and they are therefore in a strong post-burst phase. In the HR runs, there are fewer galaxies with no stars formed in the last 10 Myr, and the role of extreme post-burst galaxies is therefore smaller. 786 (176) galaxies from the HR (SR) simulations are shown.

ies for which no stars are formed within a lookback times of 10 Myr (measured from  $z = 2$ ); for these galaxies, the SFR is set equal to  $50 \times m_*/(200 \text{ Myr})$  (see Section 3.3 for details).

Overall there is a good agreement with the 16-84% percentile intervals for the HR and SR runs across all masses. The only significant difference is at  $M_* = 10^9 M_\odot$ , where the SR simulations have a significantly larger scatter than the HR simulations (this is true also for the  $M_* = 10^{8.5} M_\odot$  bin, but the difference is more modest). This is because a large fraction of the galaxies from the SR simulations in this mass bin are in a strong post-burst phase, in which no stars were formed in the last 10 Myr before the snapshot. For such galaxies, the SFR is assigned a resolution-dependent upper limit, as described above. It is intuitive that when the resolution of a simulation is increased, the amount of star formation that occurs in post-burst phases will be better resolved (because the SFR corresponding to one particle formed in a 10-Myr bin will become lower). Moreover, the scatter in the  $\text{SFR}(\text{H}\alpha)/\text{SFR}(\text{FUV})$  ratio may depend on the minimum GMC mass that can be resolved; see the next section for details. Because of this effect, it is expected that when the resolution is further increased, the amount of scatter in the  $\text{SFR}(\text{H}\alpha)/\text{SFR}(\text{FUV})$  ratio will decrease.

## 6 THE PHYSICAL CAUSES OF BURSTY STAR FORMATION IN THE FIRE SIMULATIONS

We have demonstrated that the galaxies in the FIRE simulations exhibit bursty star formation histories (except for the  $M_* > 10^{10} M_\odot$  galaxies at  $z = 0$ ) and that the level of variability is similar to observations, with the biggest difference being slightly burstier galaxies at  $M_* \lesssim 10^{9.5} M_\odot$  in the simulations. The SFRs of low-mass galaxies can vary by 1-2 orders of magnitude on timescales of order 10 Myr. These highly variable star formation histories are in

marked contrast with the smoothly varying star formation histories that are characteristic of galaxies in large-volume cosmological simulations (Sparre et al. 2015) and non-cosmological simulations that do not include resolved stellar feedback (e.g. Hayward et al. 2014a). It is thus worthwhile to ask which physical mechanisms are responsible for this difference.

One obvious reason is that in the FIRE simulations, the structure of the ISM is resolved on scales that are orders-of-magnitude less than the typical resolution of large-volume cosmological simulations. Moreover, gas is allowed to cool to 10 K, whereas effective equation of state models (e.g. Springel & Hernquist 2003) typically do not allow dense gas to cool below  $\approx 10^4$  K. Consequently, we are able to apply a star formation density threshold,  $n_{\text{crit}} = 10 \text{ cm}^{-3}$ , that is two orders of magnitude higher than that typically employed in effective equation of state models. All gas that is above the density threshold and satisfies our other star formation criteria (see Section 3) forms stars with an efficiency of 100 per cent per free-fall time. Thus, individual collapsing clouds form stars for only brief periods of time, i.e. until they are destroyed by stellar feedback. For the above reasons, star formation is more clustered in the FIRE simulations than in simulations that employ effective equation of state models; this is likely one reason for the greater time variability of star formation in the FIRE simulations.

Quantities such as the total stellar mass formed seem to be converged at the current resolution. This suggests that we are resolving the GMCs that account for the majority of the galaxies' integrated star formation. However, the simulations do not fully resolve the GMC mass function, and it is possible that not resolving low-mass GMCs is the cause of at least some of the apparent discrepancies between the simulations and observations, including the relatively large fraction of temporarily quenched galaxies (compared to Geha et al. 2012) and the  $z \approx 0$  simulated galaxies with lower  $\text{SFR}(\text{H}\alpha)/\text{SFR}(\text{FUV})$  ratios than observed (Figure 12). If the GMC mass function were fully resolved, the lowest-mass GMCs, which dominate in terms of number but not mass, might provide a relatively constant minimum SFR. Consequently, higher-resolution simulations may exhibit minimum  $\text{SFR}(\text{H}\alpha)/\text{SFR}(\text{FUV})$  values greater than those of the present simulations. This would both decrease the fraction of temporarily quenched galaxies and decrease the scatter in the  $\text{SFR}(\text{H}\alpha)/\text{SFR}(\text{FUV})$ . We will revisit this topic when ultra-high-resolution simulations are presented in future works (e.g. Wetzel et al., in prep.).

Another natural candidate for a mechanism that could result in very bursty star formation is Type II supernova feedback. When a galaxy starts to form stars, there is initially no effect from supernova feedback, and the clouds in the galaxy can continue to collapse to higher densities and rapidly form stars (as long as the other forms of stellar feedback, which turn 'on' once the first star is formed, are not sufficient to fully suppress star formation at this time). However, within  $\lesssim 10$  Myr, the first supernovae explode and deposit considerable momentum and energy into the surrounding ISM. Working in concert with the other feedback channels, this violent supernova feedback can be sufficient to destroy the star-forming clouds. In low-mass galaxies, after a burst of star formation, the supernova feedback can be sufficient to drive the bulk of the dense ISM out of the galaxy in the form of a galactic fountain, thus causing star formation to cease until the gas rains down on the galaxy and collapses again (Muratov et al. 2015). The burstiness is further increased because cosmological inflow of gas (Kereš et al. 2005; Nelson et al. 2013) is temporarily suppressed after strong burst episodes (Muratov et al. 2015). At  $z \lesssim 1$ , the FIRE galaxies with  $M_* \gtrsim 10^{10} M_\odot$  exhibit negligible outflows (Muratov

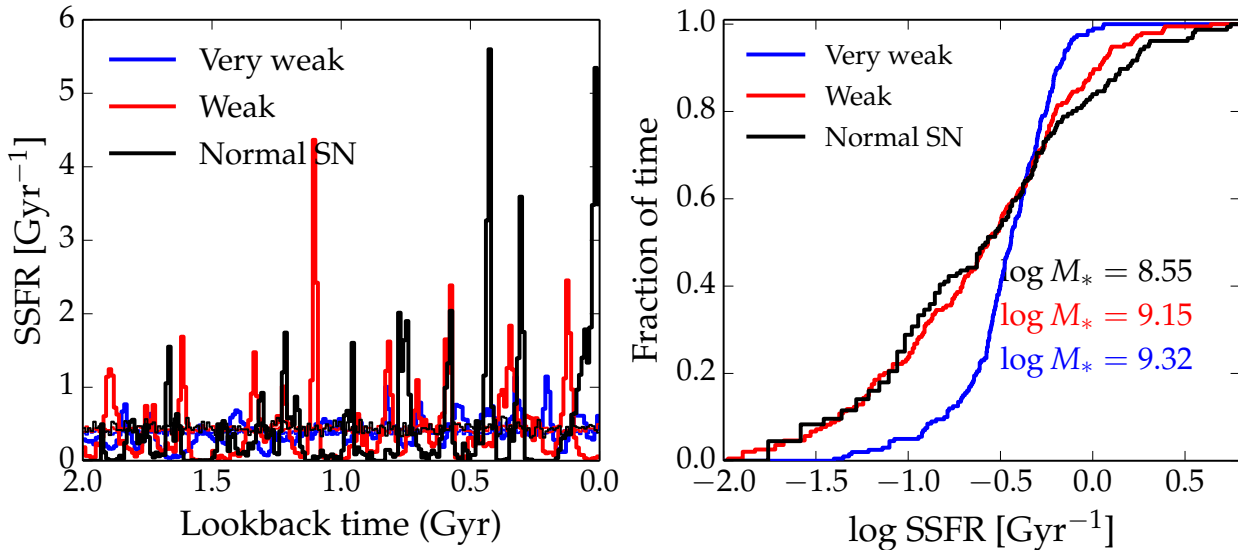


**Figure 14.** This figure shows how decreasing the role of supernova type II feedback changes the burstiness of the star formation history of the m12v halo’s central galaxy at  $z = 2$ . We here define  $\text{SSFR} \equiv \text{SFR}_{10 \text{ Myr}}/M_*(z = 2)$ . *Left panel:* The star formation histories for the m12v galaxy simulated with normal, weak and very weak Type II supernova feedback. Making supernova feedback weaker results in less bursty star formation histories. This confirms our intuition that violent supernova feedback is one of the main causes of the burstiness of the FIRE galaxies’ star formation histories.

et al. 2015), possibly because stellar-feedback-driven turbulence is no longer strong enough to generate patches of ISM with surface densities that are low enough for them to be blown out (Hayward & Hopkins, submitted). This suppression of outflows and bursty star formation (see above, especially Figure 8) in  $M_* \gtrsim 10^{10} M_\odot$  galaxies at  $z \lesssim 1$  is crucial for the emergence of well-ordered, steadily star-forming disc galaxies.

### 6.1 Runs with weaker supernova feedback

To explicitly demonstrate that Type II supernova feedback plays a dominant role in determining the burstiness of the FIRE galaxies’ star formation histories, we have performed two additional simulations of the m12v halo with supernova feedback that is weaker than in our fiducial simulation. We will examine three different simulations of the m12v halo at  $z = 2$  from Hopkins et al. (2014). The largest galaxy in the m12v-halo is quenched at  $z = 0$ , and this is the reason why we examine the star formation properties at  $z = 2$  instead. We will use runs with normal supernova feedback (*Normal SN*), *weak feedback* and *very weak feedback*. The difference between the various runs is the implementation of the sub-resolution treatment of the SN feedback (which is necessary when the Sedov–Taylor phase is not fully resolved, see Martizzi et al. 2015; Kim & Ostriker 2015; Simpson et al. 2015; Walch & Naab 2015). For the *weak* and *very weak* runs, the SN feedback is weakened by decreasing the fraction of the initial supernova ejecta energy that is converted into momentum and deposited into the surrounding gas. If  $p$  is the deposited momentum,  $p_{\text{ejecta}}$  is the ejecta momentum,  $M_{\text{enc}}(< R_{\text{cool}})$  is the enclosed ISM mass within the cooling radius, and  $M_{\text{ejecta}}$  is the mass of the ejecta, then the coupling in the standard feedback implementation is the following (see Hopkins et al. 2014 for details):

$$\frac{p}{p_{\text{ejecta}}} = \sqrt{1 + M_{\text{enc}}(< R_{\text{cool}})/M_{\text{ejecta}}}. \quad (2)$$

For the weak and very weak SN feedback runs, the right-hand side of Eq. (2) was decreased by factors of 4 and 8, respectively, which

makes it possible for us to study how the burstiness of the FIRE galaxies is influenced by supernova feedback.

The *left panel* of Figure 14 shows  $\text{SSFR} \equiv \text{SFR}_{10 \text{ Myr}}/M_*(z = 2)$  versus time for the main m12v halo in the three different simulations, and the *right panel* shows the cumulative distribution functions of the SSFR for each simulation. Because the galaxies in the FIRE simulations evolve stochastically, it is only meaningful to compare the simulations in a statistical manner (i.e. comparing the SSFR values at a fixed time is not useful). These plots reveal that when the supernova feedback is stronger, the variations in the SSFR are greater: not only is the SSFR less in the post-burst phases, but also the SSFR is greater during the bursts. Thus, this test clearly indicates that supernova feedback is one of the primary causes of the burstiness of the FIRE galaxies’ star formation histories, and it can result in bursty SFHs even in massive galaxies (m12v has a  $z = 0$  halo mass of  $\simeq 10^{12} M_\odot$ ).

It is intuitive that stronger SN feedback results in lower SSFRs in post-burst phases, but the fact that the maximum SSFR is increased may seem counter-intuitive. There are (at least) two possible reasons for this effect: (1) the stronger SN feedback causes more gas to be kicked out of the galaxy but not the halo, resulting in more prominent galactic fountains. This gas rains down on the galaxy at a later time, resulting in a higher SSFR than would occur if the SN feedback were weaker. (2) When the SN blastwaves interact with the ambient ISM, the resulting shock compression could cause triggered star formation. A detailed analysis of these two possibilities is beyond the scope of this paper, but we note that a preliminary investigation suggests that the first effect is dominant (i.e. triggered star formation does not seem to be common).

## 7 DISCUSSION

### 7.1 What we can learn from the $\text{H}\alpha$ -to-UV ratio

Understanding the observed distribution of the  $\text{H}\alpha$ -to-UV ratio is a challenging problem because several physical mechanisms



might affect this ratio. Of importance are naturally the mechanisms that alter the fraction of short-lived massive stars, which include stochastic IMF sampling, IMF variations and bursty star formation histories (Lee et al. 2009; Fumagalli et al. 2011; Eldridge 2012; Weisz et al. 2012; da Silva et al. 2014). Additionally, dust attenuation also influences the observed ratio because the UV flux is attenuated more than the  $H\alpha$  flux (see the discussion in Lee et al. 2009). Disentangling the roles of each of these effects is very difficult, but the observed ratio can still provide important constraints on each process, as we saw in Section 5.3.

Because one of the main drivers of burstiness in the FIRE simulations is supernova feedback (Figure 14), alternate implementations of supernova feedback could affect the resulting  $H\alpha$ -to-UV ratios of simulated galaxies. There is, however, not much room for modifying the supernova feedback coupling in the FIRE physics model. In dwarf galaxies, individual supernova remnants are resolved, and even in the more massive galaxies, they are time-resolved, and the subgrid model should do a reasonable job at capturing the unresolved phases (the uncertainties are at the tens of percent level; Martizzi et al. 2015).

An additional physical effect that could be implemented in simulations is stochastic IMF sampling (see Cerviño 2013 for a review). Accounting for this effect in our stellar population synthesis calculations could decrease the mean and median  $H\alpha$ -to-UV ratios and also alter the scatter in the ratio (da Silva et al. 2014). Stochastic sampling of the IMF could also alter the effectiveness of stellar feedback. SN feedback is already implemented stochastically in our simulations. However, the momentum and energy imparted by other forms of feedback from massive stars (e.g. radiation pressure) is implemented assuming full IMF sampling and thus can be ‘diluted’ on average in low-mass galaxies. By this, we mean that when a star particle is spawned, if it is not sufficiently massive, the momentum and energy deposited can be less than that associated with a single  $10 M_{\odot}$  star. If stochastic IMF sampling were implemented, the energy and momentum deposition would occur in a more spatially and temporally concentrated manner. Thus, how stochastic IMF sampling would influence our stellar feedback model is unclear, and this is a topic of ongoing work.

Given that SFR variability on short timescales can produce cored dark matter density profiles (consistent with observations; Chan et al. 2015), it is naturally important to test whether the burstiness that results from a given feedback model is consistent with observations. As we have shown, such a test can be made at  $z = 0$  by comparing the  $H\alpha$ -to-FUV flux ratios of a simulated sample of galaxies with those observed. Even though this measure is sensitive to several physical processes, one can still constrain the nature of bursty star formation cycles by requiring that the scatter in this ratio for the simulations not be larger than the observed scatter. Such comparisons will make it possible to determine whether real galaxies exhibit sufficiently violent stellar feedback to produce cored dark matter profiles.

A limitation of using the  $H\alpha$ -to-FUV flux ratio to constrain bursty star formation is that this ratio is difficult to constrain accurately for individual galaxies even at  $z = 0$ , and it is much harder to measure for high-redshift galaxies. Luckily, new instruments, such as the Multi-Object Spectrometer for Infra-Red Exploration (MOSFIRE; McLean et al. 2012) at the Keck Observatory, are making it possible to more accurately constrain this ratio by providing rest-frame-optical spectra (which are required – but not necessarily sufficient – to accurately correct for dust attenuation; Reddy et al. 2015) for thousands of high-redshift galaxies. A relevant ongoing survey is the MOSFIRE Deep Evolution Field

(MOSDEF, Kriek et al. 2015) survey. Using data from this survey and ancillary 3D-HST UV photometry (Skelton et al. 2014), the SFR– $M_*$  relation can be derived separately using both  $H\alpha$  and UV fluxes for the same galaxies (Shivaei et al. 2015). A limitation of such observations is that they mostly constrain massive galaxies ( $M_* > 10^9 M_{\odot}$ ), unlike local observations, which provide constraints down to  $M_* \simeq 10^6 M_{\odot}$ , where the effect of supernova feedback – and thus scatter in the  $H\alpha$ -to-FUV flux ratio – is predicted to be much stronger because of the shallower potentials of less-massive galaxies.

## 7.2 Bursty star formation and the scatter in the SFR– $M_*$ relation

The SFR– $M_*$  relation plays a central role in galaxy evolution phenomenology, in which the emerging picture is that galaxies build up most of their stellar mass while they are on this relation (e.g. Lilly et al. 2013) and are fuelled by continuous gas supply (Kereš et al. 2005). According to the common lore, when a merger occurs, galaxies enter the ‘starburst mode’, and this is often believed to be followed by a quenching event in which the star-forming gas not consumed in the starburst is ejected from the galaxy. In many simple analytical models, all galaxies with a given stellar mass are assumed to have the same SFR (Mitra et al. 2015), whereas in semi-analytical models, scatter in the SFR at fixed  $M_*$  is ensured by accounting for the merger and accretion histories of different halos (Henriques et al. 2015). In large-volume cosmological simulations, the gas flows in galaxies are accounted for, and the SFR varies on timescales of hundreds Myr (Sparre et al. 2015). In these three types of galaxy formation models, galaxies evolve in a quasi-equilibrium state in which the SFR fluctuates slowly with a variability timescale of  $\gtrsim 100$  Myr.

The behaviour of the galaxies in the FIRE simulations challenges this picture. In these simulations, stars are often formed in burst cycles, and it is not unusual that the SFR changes by an order of magnitude or more within a 200-Myr time interval. At  $z = 0$ , this bursty star formation mode is most evident at low masses ( $M_* < 10^9 M_{\odot}$ ), whereas at higher masses, a more steadily star-forming mode is present. In the bursty mode, galaxies quickly change from being in a burst to a post-burst phase. When using e.g. a 10-Myr-averaged SFR indicator, one will observe the short-timescale variability of these star formation cycles, but when using an SFR indicator that is sensitive to  $\gtrsim 100$  Myr timescales, one will get the impression that the galaxies are in a quasi-equilibrium with a slowly varying SFR. The observation of a tight SFR– $M_*$  relation when using long-timescale SFR indicators can be considered a consequence of the central limit theorem, from which one would expect a tight relation if galaxies are affected by many processes that act on timescales shorter than that to which the SFR indicator employed is sensitive (for a comprehensive work about the central limit theorem and the SFR– $M_*$  relation, see Kelson 2014).

It is worthwhile to ask whether signs of bursty star formation are present in existing observations of the SFR– $M_*$  relation because the scatter in the relation is expected to be larger (at least at low masses, where the burstiness of star formation is expected to be strongest) when short-timescale SFR indicators, such as  $H\alpha$ , rather than longer-timescale indicators (e.g. FUV or far-infrared) are used. To assess whether such a signature is present in actual observations, Figure 15 shows the SFR– $M_*$  relations derived using both the  $H\alpha$  and FUV fluxes from Table 1 of Weisz et al. (2012). At  $M < 10^8 M_{\odot}$ , the scatter in the SFR– $M_*$  relation is indeed larger when  $H\alpha$  is used as the SFR indicator, which we

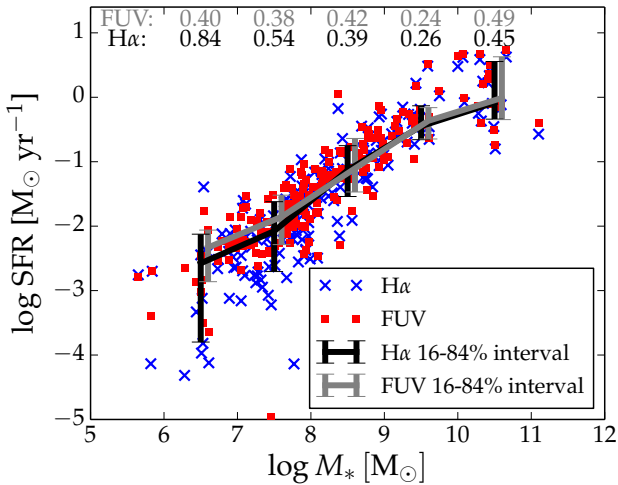


**Figure 15.** The observed SFR– $M_*$  relation at  $z = 0$  obtained using two different SFR indicators, the  $H\alpha$  and FUV luminosities (blue  $x$  symbols and red squares, respectively). The data are from Weisz et al. (2012). The median relations are denoted by the black line for  $H\alpha$  and the gray line for FUV, and the 16–84th percentile ranges are indicated by the vertical bars. In the top of the figure, the scatter in the SFR– $M_*$  relation in each mass bin is specified. For  $M_* < 10^8 M_\odot$ , the scatter is larger for the  $H\alpha$ -derived relation than for the FUV-derived relation; this difference is a potential signature of bursty star formation.

interpret as a potential signature of bursty star formation. In the  $10^6 < M_*/M_\odot < 10^7$  mass bin, if we assume that the difference in scatter between the  $H\alpha$ - and FUV-derived relations originates exclusively from bursty star formation, the scatter from bursty star formation is indeed the dominant scatter in the  $H\alpha$ -derived relation:

$$\begin{aligned} \sigma(\text{bursty SF}) &= \sqrt{\sigma^2(H\alpha) - \sigma^2(\text{FUV})} \\ &= \sqrt{0.84^2 - 0.40^2} \\ &\simeq 0.74 \text{ dex.} \end{aligned}$$

We note, however, that other effects, such as incomplete IMF sampling, could also explain the increased scatter in the observed  $H\alpha$ -derived relation.

At  $z = 2$ , no observations of the SFR– $M_*$  relation at such low masses are available, but data from the MOSDEF survey have been used to measure the scatter at higher masses,  $M_* > 10^{9.5} M_\odot$  (Shivaei et al. 2015). As we have previously discussed, it is unclear whether the observed increase in  $H\alpha$ -scatter compared to UV-scalar is due to bursty star formation or systematic uncertainties related to correcting for dust attenuation.

Looking forward, we encourage further  $z = 2$  observations that will push down the mass threshold above which the  $H\alpha$ - and FUV-derived SFR– $M_*$  relations can be measured. This would provide a useful constraint on the importance of bursty star formation in the mass range in which the SFR variability is largest in our simulations (and also according to  $z \simeq 0$  observations).

### 7.3 Limited galaxy number statistics

An important issue to keep in mind when comparing observations with the FIRE simulations is selection effects. The simulations presented in this paper are all zoom simulations of the environments around a few halos. Properties such as the scatter in the SFR– $M_*$

relation and the scatter in the SFR( $H\alpha$ )/SFR(FUV) ratio might therefore be biased by our selection of galaxies from environments that statistically differ from a cosmologically representative volume. The effect is expected to be most pronounced at  $z = 0$ , where our sample of galaxies comes from only four different zoom simulations. It is therefore likely that larger samples of simulations would alter the distribution of SFR( $H\alpha$ )/SFR(FUV) ratios at  $z = 0$ , where there is some tension between our simulated samples of galaxies and observations.

### 7.4 What about galaxy mergers?

Historically, galaxy mergers and starbursts have been closely connected concepts. Early idealised simulations of galaxy mergers indicated that the mutual tidal forces induced by the interaction could cause otherwise stable discs to develop bars, which subsequently drove strong gas inflows into the central regions of the galaxies (e.g. Negroponte & White 1983; Hernquist 1989; Mihos & Hernquist 1994b, 1996; Barnes & Hernquist 1996).<sup>7</sup> Consequently, the SFR of the system was enhanced considerably: this enhancement could be as much as two orders of magnitude for a short ( $\lesssim 100$  Myr) time near final coalescence (e.g. Barnes & Hernquist 1991; Mihos & Hernquist 1994b, 1996). Because the simulations indicated that minor mergers could also drive strong starbursts (e.g. Mihos & Hernquist 1994a), a reasonable conclusion was that the majority of disc galaxies have experienced one or more merger-driven starbursts.

In the subsequent decades since the aforementioned pioneering works, the connection between mergers and starbursts has been studied in great detail, including by some of the authors of the present work, and the concepts are still considered closely related (and sometimes even equated). Thus, it may seem surprising that mergers have received almost no mention in this work. In Section 4.2, we explicitly noted that the starbursts studied in this work are generally *not* merger-driven but rather a consequence of a combination of clustered star formation and strong stellar feedback. Nevertheless, the SFR enhancements in starbursts exhibited by the FIRE galaxies are comparable to those observed in simulations of merger-induced starbursts (see e.g. Figure 11).

Still, the results presented herein do not rule out that mergers drive strong starbursts. Rather, they indicate that except for massive ( $M_* \gtrsim 10^{10} M_\odot$ ) galaxies at low redshift ( $z \lesssim 1$ ), galaxies evolve in a quasi-equilibrium characterised by strong bursts of star formation and subsequent periods of ‘quiescence’, *even if they are not actively undergoing mergers*. However, mergers may drive additional burstiness, even for a small subset of the simulated galaxies analysed in this work. As noted by Barnes & Hernquist (1996), stellar feedback may alter the gas inflow induced by galaxy mergers and thus potentially affect the amount of SFR enhancement that results from mergers. Thus, it is still worthwhile to investigate in detail whether mergers result in starburst activity in simulations that resolve the structure of the ISM on the scales of GMCs and include explicit stellar feedback. Hopkins et al. (2013a) presented a small number of merger simulations that utilised an early version of the FIRE feedback model. They found that compared with the same initial conditions run with the Springel & Hernquist (2003) ISM model, the merger-induced starbursts were less clearly pronounced

<sup>7</sup> This possibility was suggested by Toomre & Toomre (1972) but not explicitly demonstrated until hydrodynamical simulations, rather than purely collisionless simulations, were employed.

in the simulations with resolved stellar feedback, primarily because the latter simulations exhibited significantly more short-timescale variability. There still seemed to be some SFR enhancement from the interactions, but this enhancement was not analysed in detail, and the simulation suite was by no means comprehensive. Thus, how effectively galaxy mergers drive starbursts is worthy of further (re)consideration.

## 8 CONCLUSIONS

In this paper, we studied the short-timescale variability of the SFR in the FIRE simulations by comparing the SFRs calculated using different indicators with different sensitivity timescales. Our analysis compares the SFR averaged over 10- and 200-Myr time intervals, and to compare directly to observations, we also calculated the (unattenuated) H $\alpha$ - and FUV-derived SFRs of our simulated galaxies. Our main results are the following:

- To assess whether the burstiness of our simulated galaxies' star formation histories is consistent with observations, we calculated the ratio between the H $\alpha$ - and FUV-derived SFRs. By comparing the scatter in this ratio with observations of local galaxies (within 11 Mpc of the Galaxy), we found that the burstiness of most of the FIRE galaxies' star formation histories is within the observational constraints, except for a small but non-negligible fraction of simulated galaxies with  $M_* \lesssim 10^{9.5} M_\odot$  that have lower H $\alpha$ -to-FUV ratios than observed. A signature of these galaxies is that the scatter in the SFR(H $\alpha$ )/SFR(FUV) ratio is 0.2 dex larger in the simulations than in observations. Note, however, that the simulated galaxies at  $z = 0$  come from only four different zoom simulations, so it is likely that our simulated halos are biased towards specific halo environments, which could potentially affect the statistical behaviour of the burstiness of galaxies.

- The scatter in the SFR– $M_*$  relation is sensitive to the bursty star formation histories. When using H $\alpha$ - and FUV-based SFR indicators, the scatter at  $z = 2$  is 0.48 dex and 0.37 dex, respectively. The scatter is larger for the H $\alpha$ -derived SFR because it is more sensitive to short bursts than the FUV-based indicator. The scatter in the simulated relation is slightly larger than observed (Shivaei et al. 2015 observes a scatter of 0.36 dex and 0.31 dex for H $\alpha$  and FUV, respectively), thus implying that the bursts are more pronounced in FIRE than in these observed galaxies.

- Low-mass galaxies are more bursty than high-mass galaxies. We encourage further observations that will push down the mass threshold above which the SFR– $M_*$  relation can be measured at high redshift (e.g.  $z \simeq 2$ ). Comparisons of the scatter in the observed relations based on H $\alpha$ - and FUV-derived SFRs will reveal how the burstiness of star formation depends on galaxy mass, and thereby provide useful constraints on the physics of stellar feedback.

- For low-mass galaxies ( $M_* < 10^9 M_\odot$ ), the SFR in the FIRE galaxies changes so rapidly that a galaxy can go through both (temporarily) quenched and starburst phases during a 200-Myr time interval. This result indicates that such galaxies are not evolving steadily on a 'star-forming main sequence'; instead, they have rapidly fluctuating SFRs. Observations show similar signs of rapidly fluctuating SFRs at masses of  $M_* \lesssim 10^{8.5} M_\odot$  at  $z = 0$ .

- By comparing the behaviour of the 10- and 200-Myr-averaged SFRs, we have shown that at  $z = 0$ , low-mass galaxies ( $M_* \lesssim 10^9 M_\odot$ ) spend 15-35% of their time in burst cycles, in which they form  $> 80\%$  of their stars. In more-massive galaxies ( $M_* > 10^{10} M_\odot$ ), the star formation is more steady, and burst cycles are

less important. These results are in agreement with observations that the fraction of stars formed in bursts is a declining function of stellar mass (Kauffmann 2014). At  $z = 2$ , all galaxies spend of order 20% of the time in bursts and form a significant fraction of their stellar mass in bursts, ranging from 40% for  $M_* = 10^{11} M_\odot$  to  $> 90\%$  for  $M_* < 10^7 M_\odot$ .

- The FIRE feedback model is fundamentally different from the sub-resolution physics models typically used in large-scale cosmological simulations, such as Illustris and EAGLE, in which there is very little variability in the SFR on short timescales. The bursty nature of the FIRE galaxies arises for two primary reasons: (1) the ISM is resolved on the scales of GMCs, which enables star formation to proceed in a spatially clustered and time-variable manner. Because the GMC mass function is not fully resolved in the current simulations, it is possible that at least some of the low SFR(H $\alpha$ )/SFR(FUV) ratios are artifacts of our limited resolution, despite the simulations being some of the highest-resolution cosmological simulations performed to date. (2) SN feedback disrupts star-forming clouds soon after star formation is initiated. This feedback drives strong outflows, but much of the gas later rains back down on the galaxy and leads to further star formation.

## ACKNOWLEDGEMENTS

We thank Mark Krumholz and Chuck Steidel for useful discussion. The Dark Cosmology Centre is funded by the Danish National Research Foundation. MS thanks the Sapere Aude fellowship program and acknowledges the hospitality of the California Institute of Technology. CCH is grateful to the Gordon and Betty Moore Foundation for financial support. CAFG is supported by NSF through grants AST-1412836 and AST-1517491, by NASA through grant NNX15AB22G, and by Northwestern University funds. This work was supported in part by National Science Foundation Grant No. PHYS-1066293 and the hospitality of the Aspen Center for Physics. DK was supported in part by NSF grant AST-1412153 and funds from the University of California San Diego. We also acknowledge the following computer time allocations: TG-AST120025 (PI: DK), TG-AST130039 (PI: PH), TG-AST1140023 (PI: CAFG).

## REFERENCES

- Amorisco N. C., Zavala J., de Boer T. J. L., 2014, *ApJ*, 782, L39  
 Atek H., et al., 2011, *ApJ*, 743, 121  
 Atek H., et al., 2014, *ApJ*, 789, 96  
 Barnes J. E., Hernquist L., 1996, *ApJ*, 471, 115  
 Barnes J. E., Hernquist L. E., 1991, *ApJ*, 370, L65  
 Barro G., et al., 2015, arXiv:1503.07164  
 Behroozi P. S., Wechsler R. H., Conroy C., 2013, *ApJ*, 770, 57  
 Brinchmann J., Charlot S., White S. D. M., Tremonti C., Kauffmann G., Heckman T., Brinkmann J., 2004, *MNRAS*, 351, 1151  
 Calzetti D., 2013, *Star Formation Rate Indicators*, Falcón-Barroso J., Knapen J. H., eds., *Proceedings of the XXIII Canary Islands Winter School of Astrophysics*, ArXiv: 1208.2997  
 Cerviño M., 2013, *New A Rev.*, 57, 123  
 Chan T. K., Kereš D., Oñorbe J., Hopkins P. F., Muratov A. L., Faucher-Giguère C.-A., Quataert E., 2015, arXiv:1507.02282  
 Chomiuk L., Povich M. S., 2011, *AJ*, 142, 197  
 Conroy C., 2013, *ARA&A*, 51, 393  
 da Silva R. L., Fumagalli M., Krumholz M., 2012, *ApJ*, 745, 145  
 da Silva R. L., Fumagalli M., Krumholz M. R., 2014, *MNRAS*, 444, 3275  
 Dalla Vecchia C., Schaye J., 2012, *MNRAS*, 426, 140

- Di Cintio A., Brook C. B., Macciò A. V., Stinson G. S., Knebe A., Dutton A. A., Wadsley J., 2014, *MNRAS*, 437, 415
- Domínguez A., Siana B., Brooks A. M., Christensen C. R., Bruzual G., Stark D. P., Alavi A., 2015, *MNRAS*, 451, 839
- Ekström S., et al., 2012, *A&A*, 537, A146
- Elbaz D., et al., 2011, *A&A*, 533, A119
- Eldridge J. J., 2012, *MNRAS*, 422, 794
- Erb D. K., Shapley A. E., Pettini M., Steidel C. C., Reddy N. A., Adelberger K. L., 2006, *ApJ*, 644, 813
- Faucher-Giguère C.-A., Hopkins P. F., Kereš D., Muratov A. L., Quataert E., Murray N., 2015, *MNRAS*, 449, 987
- Faucher-Giguère C.-A., Lidz A., Zaldarriaga M., Hernquist L., 2009, *ApJ*, 703, 1416
- Feldmann R., Mayer L., 2015, *MNRAS*, 446, 1939
- Franx M., van Dokkum P. G., Schreiber N. M. F., Wuyts S., Labbé I., Toft S., 2008, *ApJ*, 688, 770
- Fumagalli M., da Silva R. L., Krumholz M. R., 2011, *ApJ*, 741, L26
- Fumagalli M., et al., 2012, *ApJ*, 757, L22
- Furlong M., et al., 2015, *MNRAS*, 450, 4486
- Garrison-Kimmel S., Rocha M., Boylan-Kolchin M., Bullock J. S., Lally J., 2013, *MNRAS*, 433, 3539
- Geha M., Blanton M. R., Yan R., Tinker J. L., 2012, *ApJ*, 757, 85
- Genel S. et al., 2014, *MNRAS*, 445, 175
- Gill S. P. D., Knebe A., Gibson B. K., 2004, *MNRAS*, 351, 399
- Governato F., et al., 2010, *Nature*, 463, 203
- Hayward C. C., Smith D. J. B., 2015, *MNRAS*, 446, 1512
- Hayward C. C., Torrey P., Springel V., Hernquist L., Vogelsberger M., 2014a, *MNRAS*, 442, 1992
- Hayward C. C., et al., 2014b, *MNRAS*, 445, 1598
- Heckman T. M., Armus L., Miley G. K., 1990, *ApJS*, 74, 833
- Henriques B. M. B., White S. D. M., Thomas P. A., Angulo R., Guo Q., Lemson G., Springel V., Overzier R., 2015, *MNRAS*, 451, 2663
- Hernquist L., 1989, *Nature*, 340, 687
- Hillier D. J., Miller D. L., 1998, *ApJ*, 496, 407
- Hopkins A. M., Beacom J. F., 2006, *ApJ*, 651, 142
- Hopkins P. F., 2013, *MNRAS*, 428, 2840
- Hopkins P. F., 2014, GIZMO: Multi-method magnetohydrodynamics+gravity code. Astrophysics Source Code Library
- Hopkins P. F., 2015, *MNRAS*, 450, 53
- Hopkins P. F., Cox T. J., Hernquist L., Narayanan D., Hayward C. C., Murray N., 2013a, *MNRAS*, 430, 1901
- Hopkins P. F., Kereš D., Murray N., Hernquist L., Narayanan D., Hayward C. C., 2013b, *MNRAS*, 433, 78
- Hopkins P. F., Kereš D., Oñorbe J., Faucher-Giguère C.-A., Quataert E., Murray N., Bullock J. S., 2014, *MNRAS*, 445, 581
- Hopkins P. F., Quataert E., Murray N., 2011, *MNRAS*, 417, 950
- Hopkins P. F., Quataert E., Murray N., 2012, *MNRAS*, 421, 3488
- Ilbert O., et al., 2013, *A&A*, 556, A55
- Johnson B. D. et al., 2013, *ApJ*, 772, 8
- Kauffmann G., 2014, *MNRAS*, 441, 2717
- Kauffmann G., et al., 2003, *MNRAS*, 341, 33
- Kelson D. D., 2014, *ArXiv*: 1406.5191
- Kennicutt R. C., Evans N. J., 2012, *ARA&A*, 50, 531
- Kennicutt, Jr. R. C., 1998, *ApJ*, 498, 541
- Kereš D., Katz N., Weinberg D. H., Davé R., 2005, *MNRAS*, 363, 2
- Khandai N., Di Matteo T., Croft R., Wilkins S., Feng Y., Tucker E., DeGraf C., Liu M.-S., 2015, *MNRAS*, 450, 1349
- Kim C.-G., Ostriker E. C., 2015, *ApJ*, 802, 99
- Knapen J. H., James P. A., 2009, *ApJ*, 698, 1437
- Knollmann S. R., Knebe A., 2009, *ApJS*, 182, 608
- Kriek M., et al., 2015, *ApJS*, 218, 15
- Kroupa P., 2001, *MNRAS*, 322, 231
- Krumholz M. R., Fumagalli M., da Silva R. L., Rendahl T., Parra J., 2015, *MNRAS*, 452, 1447
- Krumholz M. R., Gnedin N. Y., 2011, *ApJ*, 729, 36
- Lee J. C., et al., 2009, *ApJ*, 706, 599
- Lee N., et al., 2015, *ApJ*, 801, 80
- Leitherer C., Ekström S., Meynet G., Schaerer D., Agienko K. B., Levesque E. M., 2014, *ApJS*, 212, 14
- Leitherer C., Ortiz Otálvaro P. A., Bresolin F., Kudritzki R.-P., Lo Faro B., Pauldrach A. W. A., Pettini M., Rix S. A., 2010, *ApJS*, 189, 309
- Leitherer C., et al., 1999, *ApJS*, 123, 3
- Lejeune T., Cuisinier F., Buser R., 1997, *A&AS*, 125, 229
- Lilly S. J., Carollo C. M., Pipino A., Renzini A., Peng Y., 2013, *ApJ*, 772, 119
- Ma X., Hopkins P. F., Faucher-Giguère C.-A., Zolman N., Muratov A. L., Keres D., Quataert E., 2015a, *ArXiv*: 1504.02097
- Ma X., Kasen D., Hopkins P. F., Faucher-Giguère C.-A., Quataert E., Kereš D., Murray N., 2015b, *MNRAS*, 453, 960
- Martin C. L., 1998, *ApJ*, 506, 222
- Martin C. L., 2005, *ApJ*, 621, 227
- Martizzi D., Faucher-Giguère C.-A., Quataert E., 2015, *MNRAS*, 450, 504
- Maseda M. V., et al., 2014, *ApJ*, 791, 17
- Mashchenko S., Wadsley J., Couchman H. M. P., 2008, *Science*, 319, 174
- McLean I. S. et al., 2012, in *Society of Photo-Optical Instrumentation Engineers (SPIE) Conference Series*, Vol. 8446, *Society of Photo-Optical Instrumentation Engineers (SPIE) Conference Series*, p. 0
- Michałowski M. J., Hayward C. C., Dunlop J. S., Bruce V. A., Cirasuolo M., Cullen F., Hernquist L., 2014, *A&A*, 571, A75
- Mihos J. C., Hernquist L., 1994a, *ApJ*, 425, L13
- Mihos J. C., Hernquist L., 1994b, *ApJ*, 431, L9
- Mihos J. C., Hernquist L., 1996, *ApJ*, 464, 641
- Mitra S., Davé R., Finlator K., 2015, *MNRAS*, 452, 1184
- Muratov A. L., Keres D., Faucher-Giguère C.-A., Hopkins P. F., Quataert E., Murray N., 2015, *ArXiv*: 1501.03155
- Negroponte J., White S. D. M., 1983, *MNRAS*, 205, 1009
- Nelson D., Vogelsberger M., Genel S., Sijacki D., Kereš D., Springel V., Hernquist L., 2013, *MNRAS*, 429, 3353
- Noeske K. G., et al., 2007, *ApJ*, 660, L43
- Oñorbe J., Boylan-Kolchin M., Bullock J. S., Hopkins P. F., Kereš D., Faucher-Giguère C.-A., Quataert E., Murray N., 2015, *ArXiv*: 1502.02036
- Oppenheimer B. D., Davé R., 2006, *MNRAS*, 373, 1265
- Pacifici C. et al., 2015, *MNRAS*, 447, 786
- Pacifici C., Kassin S. A., Weiner B., Charlot S., Gardner J. P., 2013, *ApJ*, 762, L15
- Pauldrach A. W. A., Hoffmann T. L., Lennon M., 2001, *A&A*, 375, 161
- Pontzen A., Governato F., 2012, *MNRAS*, 421, 3464
- Portegies Zwart S. F., McMillan S. L. W., Gieles M., 2010, *ARA&A*, 48, 431
- Read J. I., Agertz O., Collins M. L. M., 2015, *ArXiv*: 1508.04143
- Reddy N. A. et al., 2015, *ApJ*, 806, 259
- Robitaille T. P., Whitney B. A., 2010, *ApJ*, 710, L11
- Rodighiero G., et al., 2011, *ApJ*, 739, L40
- Rodighiero G., et al., 2014, *MNRAS*, 443, 19
- Sanders D. B., Mirabel I. F., 1996, *ARA&A*, 34, 749
- Scannapieco C., et al., 2012, *MNRAS*, 423, 1726
- Schaye J., et al., 2015, *MNRAS*, 446, 521
- Schmidt M., 1959, *ApJ*, 129, 243
- Shivaei I., et al., 2015, *ArXiv*: 1507.03017
- Simha V., Weinberg D. H., Conroy C., Dave R., Fardal M., Katz N., Oppenheimer B. D., 2014, *arXiv*: 1404.0402
- Simpson C. M., Bryan G. L., Hummels C., Ostriker J. P., 2015, *ApJ*, 809, 69
- Skelton R. E. et al., 2014, *ApJS*, 214, 24
- Smith D. J. B., Hayward C. C., 2015, *MNRAS*, 453, 1597
- Snyder G. F., Cox T. J., Hayward C. C., Hernquist L., Jonsson P., 2011, *ApJ*, 741, 77
- Sparre M., et al., 2015, *MNRAS*, 447, 3548
- Speagle J. S., Steinhardt C. L., Capak P. L., Silverman J. D., 2014, *ApJS*, 214, 15
- Springel V., 2005, *MNRAS*, 364, 1105
- Springel V., Hernquist L., 2003, *MNRAS*, 339, 289
- Springel V., Yoshida N., White S. D. M., 2001, *New Astronomy*, 6, 79

- Stinson G., Seth A., Katz N., Wadsley J., Governato F., Quinn T., 2006, MNRAS, 373, 1074
- Teyssier R., Pontzen A., Dubois Y., Read J. I., 2013, MNRAS, 429, 3068
- Thompson T. A., Quataert E., Murray N., 2005, ApJ, 630, 167
- Toomre A., Toomre J., 1972, ApJ, 178, 623
- Torrey P., Cox T. J., Kewley L., Hernquist L., 2012, ApJ, 746, 108
- Torrey P., Vogelsberger M., Genel S., Sijacki D., Springel V., Hernquist L., 2014, MNRAS, 438, 1985
- Tremonti C. A. et al., 2004, ApJ, 613, 898
- Utomo D., Kriek M., Labbé I., Conroy C., Fumagalli M., 2014, ApJ, 783, L30
- Vázquez G. A., Leitherer C., 2005, ApJ, 621, 695
- Vogelsberger M., Genel S., Sijacki D., Torrey P., Springel V., Hernquist L., 2013, MNRAS, 436, 3031
- Vogelsberger M., et al., 2014, Nature, 509, 177
- Walch S., Naab T., 2015, MNRAS, 451, 2757
- Walcher J., Groves B., Budavári T., Dale D., 2011, Ap&SS, 331, 1
- Weisz D. R. et al., 2011, ApJ, 739, 5
- Weisz D. R., Dolphin A. E., Skillman E. D., Holtzman J., Gilbert K. M., Dalcanton J. J., Williams B. F., 2014, ApJ, 789, 147
- Weisz D. R., Skillman E. D., Cannon J. M., Dolphin A. E., Kennicutt, Jr. R. C., Lee J., Walter F., 2008, ApJ, 689, 160
- Weisz D. R., et al., 2012, ApJ, 744, 44
- Wheeler C., Oñorbe J., Bullock J. S., Boylan-Kolchin M., Elbert O. D., Garrison-Kimmel S., Hopkins P. F., Kereš D., 2015, MNRAS, 453, 1305
- Williams B. F. et al., 2015, ApJ, 806, 48
- Williams R. J., Quadri R. F., Franx M., van Dokkum P., Toft S., Kriek M., Labbé I., 2010, ApJ, 713, 738
- Zolotov A., et al., 2012, ApJ, 761, 71